Ⓔ

AXISYMMETRIC DYNAMICAL MODELS OF THE CENTRAL REGIONS OF GALAXIES

Karl Gebhardt,[1] Douglas Richstone,[2] Scott Tremaine,[3] Tod R. Lauer,[4] Ralf Bender,[5]
Gary Bower,[6] Alan Dressler,[7] S. M. Faber,[8] Alexei V. Filippenko,[9] Richard Green,[4]
Carl Grillmair,[10] Luis C. Ho,[7] John Kormendy,[1] John Magorrian,[11]
and Jason Pinkney[2]

ABSTRACT

We present axisymmetric, orbit superposition models for 12 galaxies using data taken with the *Hubble Space Telescope* (*HST*) and ground-based observatories. In each galaxy, we detect a central black hole (BH) and measure its mass to accuracies ranging from 10% to 70%. We demonstrate that in most cases the BH detection requires *both* the *HST* and ground-based data. Using the ground-based data alone does provide an unbiased measure of the BH mass (provided that they are fitted with fully general models), but at a greatly reduced significance. The most significant correlation with host galaxy properties is the relation between the BH mass and the velocity dispersion of the host galaxy; we find no other equally strong correlation and no second parameter that improves the quality of the mass-dispersion relation. We are also able to measure the stellar orbital properties from these general models. The most massive galaxies are strongly biased to tangential orbits near the BH, consistent with binary BH models, while lower mass galaxies have a range of anisotropies, consistent with an adiabatic growth of the BH.

Subject headings: black hole physics — galaxies: general — galaxies: nuclei — galaxies: statistics — stellar dynamics

On-line material: color figures

1. INTRODUCTION

Most nearby galaxies contain massive compact dark objects at their centers. The number density and masses of these objects are consistent with the hypothesis that they are dead quasars: massive black holes (BHs) that grew mainly by gas accretion and were once visible as quasars or other active galactic nuclei (AGNs) from radiation emitted during the accretion process (see Kormendy & Richstone 1995 for a review).

We have obtained *Hubble Space Telescope* (*HST*) spectra of the centers of 12 nearby galaxies, using first the square aperture of the Faint Object Spectrograph (FOS) and later the long slit on the Space Telescope Imaging Spectrograph (STIS). Additional ground-based spectra have been obtained at the MDM Observatory. Pinkney et al. (2002) describe the data collected by our group for the 10 galaxies observed with STIS, and we present the data for the two galaxies observed with FOS in the Appendix of this paper. In § 2 we discuss how we incorporate the data into the dynamical models.

An overall discussion of the dynamical modeling methods is given in Gebhardt et al. (2000a) and D. Richstone et al. (2003, in preparation). The models are axisymmetric and based on superposition of individual stellar orbits. In § 3 we provide the details of the models for these galaxies. Five other galaxies have stellar dynamical data and models of comparable quality. Three of these are from the Leiden Group: M32 (van der Marel et al. 1998; Verolme et al. 2002), NGC 4342 (Cretton & van den Bosch 1999), and IC 1459 (Cappellari et al. 2002). The remaining two are NGC 3379 (Gebhardt et al. 2000a) and NGC 1023 (Bower et al. 2001). Results from these five additional galaxies are included in the analysis in § 4.

We use orbit-based models rather than parameterized models of the distribution function because parameterization can lead to biased BH mass estimates. Parameterized models can even imply the presence of a BH when none exists. Orbit-based models do not suffer from this bias. However, we do make various assumptions whose consequences must be examined (§ 5). In particular, we model galaxies as axisymmetric. Triaxial and, worse yet, asymmetric galaxies may be poorly represented by axisymmetric models. However, these effects are likely to be random; therefore, it is reasonable to expect that the assumption of axisymmetry will not cause an overall bias in the BH mass.

In addition to measuring the BH mass ($M_{\rm BH}$) and stellar mass-to-light ratio (M/L, assumed to be independent of position), our models constrain the orbital structure in the galaxy. It appears from this study and those of Verolme

[1] Department of Astronomy, University of Texas at Austin, RLM 15.308, Austin, TX 78712; gebhardt@astro.as.utexas.edu, kormendy@astro.as.utexas.edu.

[2] Department of Astronomy, University of Michigan at Ann Arbor, 830 Dennison, 501 East University Avenue, Ann Arbor, MI 48109; dor@astro.lsa.umich.edu, jpinkney@astro.lsa.umich.edu.

[3] Princeton University Observatory, Peyton Hall, Princeton, NJ 08544; tremaine@astro.princeton.edu.

[4] National Optical Astronomy Observatory, P.O. Box 26732, Tucson, AZ 85726; green@noao.edu, lauer@noao.edu.

[5] Universitäts-Sternwarte, Scheinerstrasse 1, Munich 81679, Germany; bender@usm.uni-muenchen.de.

[6] Computer Sciences Corporation, Space Telescope Science Institute, 3700 San Martin Drive, Baltimore, MD 21218; bower@stsci.edu.

[7] Observatories of the Carnegie Institution of Washington, 813 Santa Barbara Street, Pasadena, CA 91101; dressler@ociw.edu, lho@ociw.edu.

[8] University of California Observatories, Lick Observatory, University of California, Santa Cruz, CA 95064; faber@ucolick.org.

[9] Department of Astronomy, University of California at Berkeley, 601 Campbell Hall, Berkeley, CA 94720-3411; alex@astro.berkeley.edu.

[10] *SIRTF* Science Center, 770 South Wilson Avenue, Pasadena, CA 91125; carl@ipac.caltech.edu.

[11] Department of Physics, University of Durham, Rochester Building, Science Laboratories, South Road, Durham DH1 3LE, UK; john.magorrian@durham.ac.uk.

et al. (2002) and Cappellari et al. (2002) that the distribution function in axisymmetric galaxies depends on all three integrals of motion, not just the energy and angular momentum.

Preliminary BH masses for these galaxies have been reported by Gebhardt et al. (2000b); these masses are based on a coarser grid of models (explained in § 4) and thus have larger uncertainties than those presented here. However, the best-fit values for the BH masses are nearly the same in the two studies.

Most distances in this paper have been measured with the surface brightness fluctuation (SBF) method (Tonry et al. 2000); for those galaxies without an SBF distance we assume the distance in an unperturbed Hubble flow and $H_0 = 80 \, \mathrm{km \, s^{-1} \, Mpc^{-1}}$.

2. DATA

The data consist of images and spectra from ground-based and *HST* observations. The high spatial resolution of *HST* is essential to measure the mass of the central BH. The ground-based data are essential to constrain the stellar orbital distribution and mass-to-light ratio. Since we are using two-dimensional galaxy models, we must have data along various position angles to constrain adequately the orbital structure.

2.1. *Imaging*

Most of the sample galaxies were imaged with WFPC2 during *HST* Cycles 4 and 5; the exception is NGC 4697, which was observed with WFPC1 (see Lauer et al. 1995). In general, each galaxy was observed in both the F555W (V) and F814W (I) filters. The typical total integration time in each filter was $\sim$1200 s, but subdivided into shorter exposures to allow for the identification of cosmic-ray events. The exposure levels at the centers of all galaxies exceeded 10^4 photons pixel^{-1} and were often nearly an order of magnitude higher. After the subexposures were compared to detect and eliminate cosmic-ray events, they were combined and then deconvolved using Lucy (1974) and Richardson (1972) deconvolution. The point-spread functions (PSFs) were provided by standard-star observations obtained during the routine photometric monitoring of WFPC2. Typically, 40 iterations of Lucy-Richardson deconvolution were used. Lauer et al. (1998) demonstrate that this procedure allows accurate recovery of the intrinsic galaxy brightness distribution for all but the central pixel. Brightness profiles were then measured from the deconvolved images using the high-resolution Fourier isophote-fitting program of Lauer (1985). The present work uses the V-band profiles, given their intrinsically higher spatial resolution. The *HST* imaging provides adequate coverage out to around 10″; beyond that we rely on ground-based imaging to complete the radial coverage. Ground-based imaging comes primarily from Peletier et al. (1990).

Figure 1 presents the luminosity density profiles of the galaxies, which are input to the dynamical models. We determine the luminosity density distribution from the surface brightness distribution by assuming that the luminosity density is axisymmetric and constant on similar spheroids. (In one galaxy, NGC 4473, we have included a stellar disk in addition to the spheroidal luminosity distribution.) We use the nonparametric techniques described by Gebhardt et al.
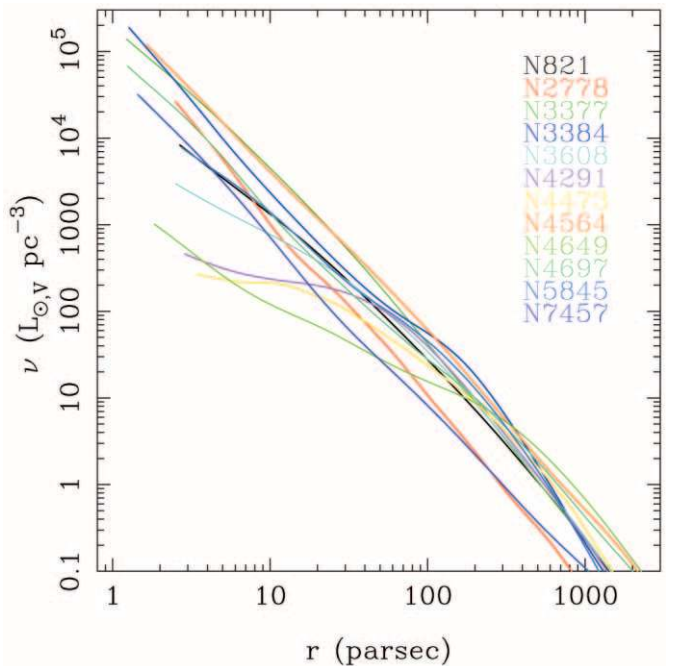

Fig. 1.—Luminosity density profiles for the sample galaxies. These are in the V band and include both *HST* and ground-based data. The radii are along the semimajor axis.

(1996), which involve smoothing the surface brightness and then inverting the Abel integral equation that relates surface brightness and luminosity density. We note that without this or some other restrictive assumption on the shape of the equidensity surfaces, the deprojection is not unique, except for edge-on galaxies (Gerhard & Binney 1996; Kochanek & Rybicki 1996). In particular, Magorrian & Ballantyne (2001) show that deprojection uncertainties, and in particular face-on disks, can significantly increase the uncertainties in the measured orbital distribution. We do not attempt a complete treatment of deprojection uncertainties in this paper, but we do discuss possible consequences and biases in § 4.9.

2.2. *HST Kinematics*

Pinkney et al. (2002) present the spectra and kinematics from the *HST* STIS observations. Most of the galaxies in our sample have spectra taken with STIS, except for NGC 3377 and NGC 5845, which were observed with a single FOS aperture. The kinematic results for these two galaxies are presented in the Appendix. We use the line-of-sight velocity distributions (LOSVDs) in the modeling (i.e., we fit to the binned LOSVD, not its moments). For most of the galaxies, we use 13 equally spaced velocity bins to represent the LOSVD. The width of the velocity bins is generally around 40% of the galaxy's velocity dispersion. The uncertainty in the signal in each velocity bin is determined using Monte Carlo simulations. We reproduce a sample of the velocity profiles in Figure 2 (for NGC 4564).

The LOSVD can be biased by several systematic effects, including the choice of stellar template, continuum shape, spectral range used in the fit, and amount of smoothing. These are discussed by Pinkney et al. (2002). In general, the most significant bias is probably template mismatch. However, most of our data are observed in the Ca II near-triplet
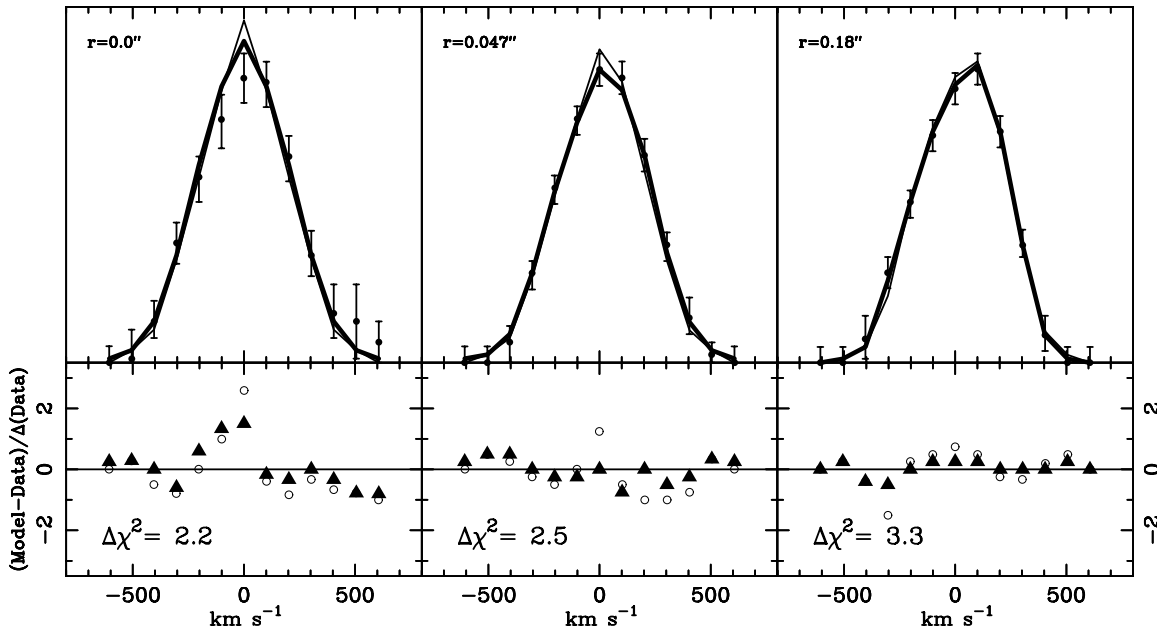
Fig. 2.—Comparison of the LOSVD from three of the 33 velocity profiles in NGC 4564; the radii are given in the upper left-hand corner of each panel. In the upper panels, the filled circles with error bars represent the data LOSVDs. The lines in the upper panels represent two different models, and the lower panels show their residuals from the data normalized by dividing by the uncertainty in the data. The thick line and triangles are the values from the best-fit BH model; the thin line and open circles are the model without a BH. The $\Delta\chi^2$ value given at the bottom is the difference between the best-fit model and the zero BH mass model for that particular bin. These three bins contribute a total of $\Delta\chi^2 = 8.0$, whereas the difference from the full sample is 52.7. [*See the electronic edition of the Journal for a color version of this figure.*]

region (8500 Å), and in this region the LOSVD is not very sensitive to template variations.

There is scattered light in STIS that is about 0.2% of the incoming light. The scattering occurs after the light has passed through the grating and so is not due to the PSF of *HST*. We measure this light using the spectral lamp images where we can use the high signal-to-noise ratio (S/N) to study the wings of the profile. There is a broad component that has a standard deviation equal to 25 pixels, presumably due to scattering in the STIS optics. We have run extensive tests to determine whether this scattered light affects our results. It is possible that a bright nucleus can scatter light into neighboring pixels that would not be reflected in the assumed PSF. We simulate this effect in both NGC 3377 (a power-law galaxy) and M87 (a core galaxy). We simulate the two-dimensional image by inputting kinematic profiles consistent with those measured in both galaxies and then convolving those kinematics with both the narrow and broad components of the PSF. We then extract and fit the profiles, ignoring the broad component, and compare with the input values. There was essentially no effect in M87, as expected since its kinematic profile does not vary strongly with radius. For NGC 3377, the change in the second moment was negligible; however, the velocity profile showed a 5% reduction in peak amplitude and the dispersion profile showed a 5% increase near the center. Since the second moment was hardly changed, this broad component has no effect on the measured BH mass and is not included in subsequent analysis.

The STIS spectral resolution with the G750M grating is around 55 km s^{-1} (FWHM), with 37 km s^{-1} per binned pixel (we bin 2 × 1 pixels on the chip for most of our data). Since we always use a template star convolved with the LOSVD to match the galaxy spectrum, we do not have to worry as

much about the detailed shape of the spectral PSF (as opposed to understanding the spatial PSF) because the velocity dispersions of our galaxies are much larger than the spectral FWHM. The main concern is whether we are illuminating the slit with the templates in the same way that we illuminate with the galaxy. For galaxies with pointlike nuclei this is not a concern, but for those with shallow light profiles we must consider the effect. The concern is whether the velocity variation across the slit adds to the dispersion measured in the galaxy, which would not be true for a point source. We can calculate the effect using the results of Bower et al. (2001). For the 0″.1 slit, the velocity variation from slit edge to edge is around 20 km s^{-1}, and for the 0″.2 slit it is 40 km s^{-1}. Given the FWHM of the spectral lines, 55 km s^{-1}, the velocity variation provides a 7%–25% increase in the required instrumental spectral FWHM. However, for the galaxies where this effect is the largest (i.e., the core galaxies), the galaxy dispersion is the greatest and therefore the broadening in the galaxy is insignificantly affected by the exact instrumental profile. For example, in the case of NGC 3608, the central dispersion is 300 km s^{-1}; with a change in the instrumental dispersion from 20 to 25 km s^{-1} (25% higher), the inferred galaxy dispersion differs by only 0.1%. Given the insignificant difference, we apply no correction for illumination effects. Bower et al. (2001) find a similar result for NGC 1023.

2.3. *Ground-based Kinematics*

Nearly all of the ground-based data come from the MDM Observatory (Pinkney et al. 2002). Briefly, most of the spectra were taken around the Ca II triplet (near 8500 Å), and the rest were taken near the Mg *b* region (5100 Å). The instrumental resolution varied slightly from run to run but was generally around 40 km s^{-1}, which is more than

adequate given the dispersions of the galaxies studied. The spatial resolution varied from $0.''5$ to $1.''5$. We included the appropriate spatial PSF for each of the ground-based spectra in the modeling.

In an axisymmetric system, the velocity profile at a radius on one side of the galaxy will be identical to a profile that is flipped about zero velocity on the other side of the galaxy at the same radius. There are three options that we can use to include this symmetry in the models. First, we can fit the same, but appropriately flipped, observed velocity profile on the two spectra from opposite sides of the galaxy during the extraction. In this way, we only include one profile at a given radius. Second, we can independently fit velocity profiles from opposite sides of the galaxy and then average these two velocity profiles (after flipping one of them) to provide one profile for that radius. Third, we can include the two independently fitted velocity profiles directly into the models. Each of these has their own advantages and disadvantages. For example, if there is a bad spot on the detector or a star on one side of the galaxy, then the most reliable measure would be to use the third option (since one can then exclude the affected region).

We have tried all three methods and find little differences between the results. We choose to use the first option since, in that case, the S/N used for the extraction of the velocity profile is increased by $\sqrt{2}$ compared to the other cases, and this serves to alleviate potential biases. This increase arises because we use two spectra to measure one velocity profile, as opposed to measuring two independent velocity profiles. The uncertainty (and, hence, the S/N) in the resultant velocity profile is the same regardless of the method used to estimate it, but our reason for using the first option is motivated by alleviating potential biases in the extraction of the velocity profile. For low-S/N data, there are often biases in the velocity profile (mainly due to the need to use more smoothing as the signal is lowered), and we decrease these biases by forcing axisymmetry during the spectral extraction. The alternative of using individual profiles from both sides of the galaxy is not optimal.

3. DYNAMICAL MODELS

D. Richstone et al. (2003, in preparation) provide a complete account of the construction of the dynamical models, including analytic tests. Here we provide a basic summary and include the details that are specific to these galaxy models. Other groups discuss the use of and tests for similar orbit-based models (van der Marel et al. 1998; Cretton & van den Bosch 1999; Cretton et al. 1999; Cretton, Rix, & de Zeeuw 2000; Cappellari et al. 2002; Verolme & de Zeeuw 2002; Verolme et al. 2002). These studies used models similar to each other; the models presented here and in Gebhardt et al. (2000a) differ from those above in small but important ways. As discussed in D. Richstone et al. (2003, in preparation), our models use a maximum likelihood approach to find the orbital weights as opposed to using a regularization method, and ours also use the full LOSVD as opposed to using parameterized moments. There are positives and negatives associated with the different approaches, and a full comparison can only be studied when the different models are applied to identical data sets.

The dynamical models are constructed as follows: We first determine the luminosity density from the surface brightness profile. Although we have constructed models with a variety of inclinations, we generally assume that the galaxy is edge-on, for reasons given in § 4. In this case, the deprojection is unique. To determine the potential, we assume a stellar mass-to-light ratio and a BH mass. In this potential we run a representative set of orbits (typically 7000) that cover phase space adequately. We then find the nonnegative set of weights for those orbits that provides the best match to the available data (in the sense of minimum χ^2). In order to have a smooth phase-space distribution, we use a maximum entropy method as described below. We repeat this analysis for different BH masses and different mass-to-light ratios to find the overall best fit.

We measure the velocity moments of our models on a two-dimensional grid in radius and angle relative to the symmetry axis of the galaxy. We generally use 20 radial and five angular grid elements. The parameters of this grid (spacing and extent) are designed to maximize the S/N in both the kinematics and the photometry. The angular bins have centers at latitudes $5.°8$, $17.°6$, $30.°2$, $45.°0$, and $71.°6$, where the angle is defined from the major to the minor axis; we use the same binning scheme whether we are in projected or internal space. We have run tests in which we both double and halve the number of bins, and we find insignificant differences. Since STIS provides kinematic information along a slit, we need to specify how to extract the data along that slit to optimize the S/N to measure the BH mass. Pinkney et al. (2002) describe the 20 radial extraction windows that we use. We define our radial binning scheme in the models with the same configuration as that used in the data extraction.

We specify the galaxy potential and the forces on a grid that is 5 times finer than the grids used in the data comparisons, in order to assure accurate orbit integration. If we have N radial bins, labeled $i = 1, \ldots, N$, our goal is to have at least one orbit with apocenter and pericenter in every possible pair of bins (i, j) in order to cover phase space well; this requires $N(N - 1)/2$ orbits, times 2 to include stars with the opposite sign of rotation. This leads to 380 orbits; however, we must also cover the angular dependence, and to do this, we include 20 additional angular bins. Thus, the total number of orbits is around 7000. We track the velocity information by storing the LOSVD for each orbit in each grid element. For each galaxy we use 13 velocity bins, spanning the maximum and minimum velocities generated for the whole orbit distribution. It is important to include all velocity information, particularly in the LOSVD wings where the effects from the BH are the strongest. Our final models consist of 7000 (orbits) $\times$ 20 (radial) $\times$ 5 (angular) $\times$ 13 (velocity) elements. For each galaxy, we generally try about 10 different BH masses, 10 or more values of M/L, and sometimes a few different inclinations. We have also run models where we have both doubled and halved the number of orbits. In either case, we find no difference in the best fit to the data.

In addition to the projected quantities, we track the internal properties including the velocity moments and luminosity density. For the dynamics, we only track the zeroth, first, and second moments of the velocity profile. The internal moments are presented in § 4.7.

It is important to include the effects of the PSF of *HST* in the dynamical models. We use the same PSF as measured by Bower et al. (2001), which has FWHM $= 0.''08$ along the slit at 8500 Å. At 8500 Å, the first diffraction peak is visible and is included in the PSF model. This profile comes from a highly sampled PSF using a cut in the spatial direction for a

star at various columns on the chip. Since there is a six-row shift of the star across the STIS chip, the PSF is sampled differently in each column, thereby producing a well-sampled profile. Unfortunately, this procedure only produces a PSF in one dimension (along the slit), and we have no measurement of the PSF in the spectral direction. As discussed by Bower et al. (2001), the PSF is expected to be circularly symmetric, so we assume that the PSF across the slit is the same as the PSF measured along the slit. We run all orbit libraries with no PSF included and then convolve with the appropriate PSF before we fit to the kinematic data. In this way, we can include a different PSF for each kinematic observation, if necessary.

We have ground-based kinematic data along two to four position angles for each galaxy, covering over half of the radial bins. Thus, we typically have 20 positions on the sky, each with 13 LOSVD bins, for a total of 260 data bins. However, as explained by Gebhardt et al. (2000a) and discussed further in § 4.1, the number of degrees of freedom is difficult to estimate. The main problem is that the smoothing in the LOSVD estimation introduces covariance between velocity bins. For a typical galaxy, every two velocity bins are correlated. This factor of 2 is determined through simulations where we vary the smoothing parameter in the velocity profile estimate and measure the effect on χ^2 (see Gebhardt et al. 2000a). Thus, the number of degrees of freedom is reduced by a factor of roughly 2 compared to the total observed parameters.

The orbit weights are chosen so that the luminosity density in every spatial bin matches the observations to better than 1%. Typically, the match is better than 0.1%. We regard matching the luminosity density in each bin as a set of constraints, rather than a set of data points. Thus, the photometric data do not contribute to the total number of degrees of freedom. We make this choice for two reasons: first, the uncertainties in the photometry are much smaller than those in the kinematics; second, including photometric uncertainties would require compiling a far larger set of orbit libraries (one for each tested photometric profile).

To ensure that the phase-space distribution function is smooth, we maximize the entropy as in Richstone & Tremaine (1984). We do this by defining a function $f \equiv \chi^2 - \alpha S$, where χ^2 is the sum of squared residuals to the data, S is the entropy, and α is a parameter describing the relative weights of entropy and residuals in the fit. Our goal is to minimize f. We start with a large value of α and then gradually reduce it until further improvement in χ^2 is no longer possible. At first, the entropy determines the orbital weights, but at the end of the minimization, the entropy has no influence on the quality of the fit. The entropy constraint does affect those regions where we do not have kinematic data, but we never use results from those regions. Solving for the 7000 orbital weights with 200–500 observations is the most computationally expensive part of the analysis. We have tried a variety of initial conditions for the orbital weights and entropy forms and find that neither the minimum value of χ^2, nor the BH mass and stellar mass-to-light ratio, nor the orbital structure is sensitive to these choices.

We need to determine the uncertainties in the BH mass and the stellar M/L. These are correlated, of course, and we generally use two-dimensional χ^2 distributions to determine the uncertainties. The uncertainties in the parameters are determined from the change in χ^2 as we vary one of the variables; in this case, the 68% confidence band is reached when

χ^2 increases above its minimum value by 1. This parameter estimation is different from hypothesis testing: a tested hypothesis is consistent with the data if χ^2 per degree of freedom is approximately unity, while the allowed range of a parameter is determined by the change in χ^2 from its minimum value. For example, since the BH has no effect on the kinematics at large radii, we could always ensure that a galaxy is consistent with the hypothesis that there is no BH by adding more and more kinematic data at large radii.

Thus, we advocate that one must use $\Delta\chi^2$ in order to determine the uncertainties in the parameters. This conclusion was also discussed in both van der Marel et al. (1998) and Cretton et al. (2000). The difficulty for the parameter estimation is that we need to measure the uncertainties in the kinematics accurately. The uncertainties on the kinematics are difficult to quantify; problems due to template mismatch and continuum estimation, for example, can have a significant effect on the results. We have tried to take this into account during the Monte Carlo simulations that we use to generate the errors. A more natural approach would be to use a Bayesian analysis, but given the large number of unknown variables (the 7000 orbital weights), this is impractical.

Figure 2 shows the data/model comparison for three LOSVDs in NGC 4564. For this galaxy, we actually have 33 velocity profiles but only show three here. Thus, there are significantly more data that have gone into the models. For NGC 4564, the signature for the BH comes from the central few bins in each of the three position angles. However, it is only by examining the full data set that one can understand the global fit for any particular model. The change in χ^2 is given in the bottom panels. The difference between the best-fit BH and zero BH model in just these three bins is equal to 8. Using the full data set, the difference is 53, implying an extremely high significance against the zero BH model.

4. RESULTS

The three main properties that we obtain from the models are the BH mass, mass-to-light ratio, and the orbital structure. The BH mass and mass-to-light ratio are fitted by choosing a grid of parameters for them and then examining their χ^2 distribution. The orbital structure, however, results from finding the orbital weights for each specified potential (i.e., BH mass and mass-to-light ratio) that provides the minimum χ^2. Each BH mass/mass-to-light ratio pair produces a best-fit orbital structure, but the overall best model is that which has the one global minimum. In this section we discuss results for each parameter and consider possible biases and additional uncertainties.

4.1. BH Mass and Mass-to-Light Ratio

Figure 3 presents χ^2 as a function of BH mass and M/L. The contours are drawn using a two-dimensional smoothing spline (Wahba 1990). As in Wahba (1990), generalized cross validation determines the smoothing value; however, the modeled values are relatively smooth and little smoothing is necessary. We plot only those points near the χ^2 minimum; we have tried many more models that lie outside the limits shown in the plot but only highlight the center to show the contour shape. Models that lie outside these limits are excluded at much greater than 99% confidence. Each approximately vertical sequence represents models with the
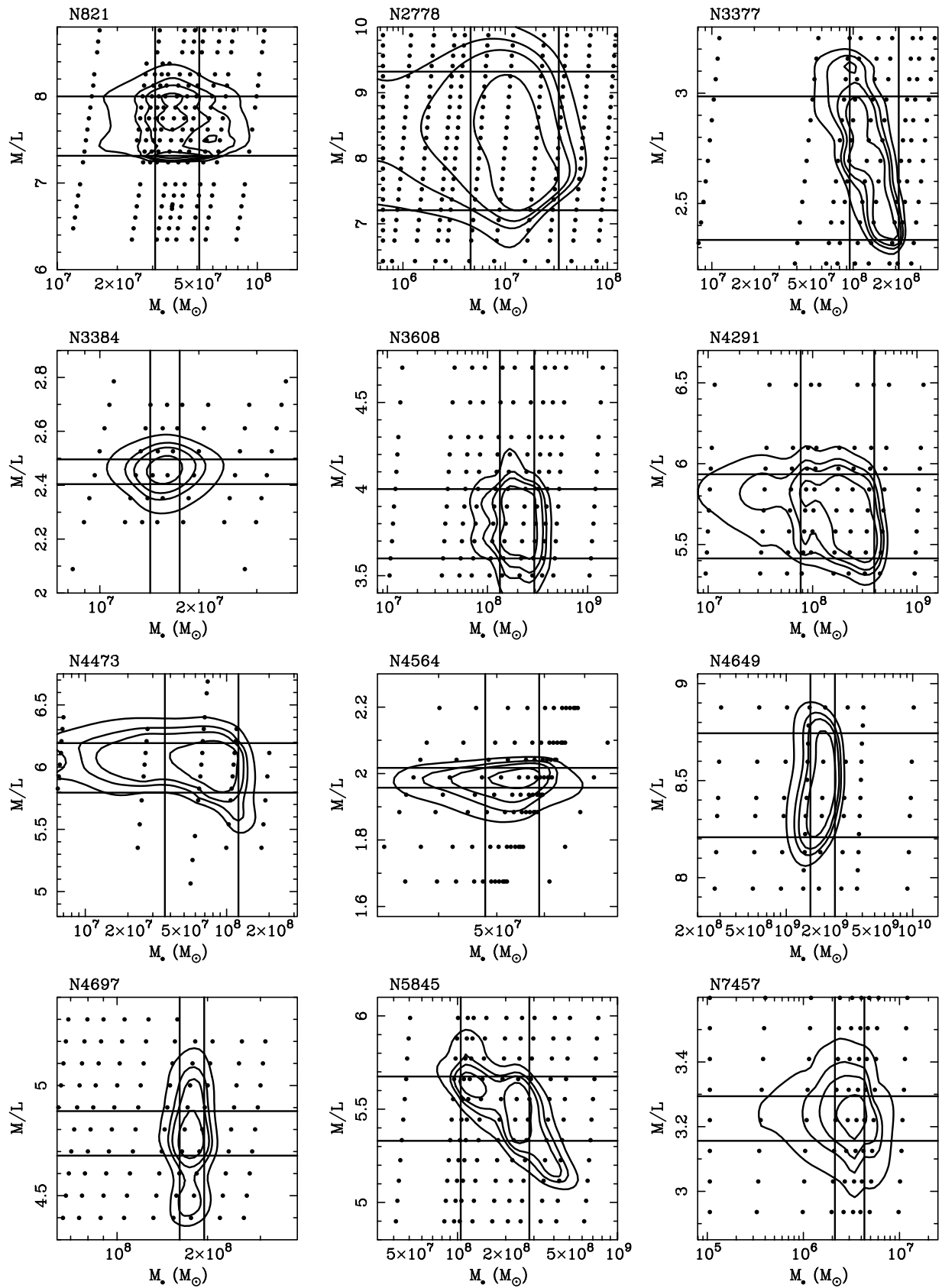
Fig. 3.—Two-dimensional plots of χ^2 as a function of BH mass and mass-to-light ratio for each of the galaxies. The points represent models that we ran. The contours were determined by a two-dimensional smoothing spline interpolated from these models and represent $\Delta\chi^2$ of 1.0, 2.71, 4.0, and 6.63 (corresponding to 68%, 90%, 95%, and 99% for 1 degree of freedom). The vertical lines are the 68% limits for the BH masses marginalized over mass-to-light ratio, and the horizontal lines are the 68% limits for the mass-to-light ratios marginalized over BH mass. [*See the electronic edition of the Journal for a color version of this figure.*]

same ratio of BH mass to galaxy mass (or M/L), all of which can use the same orbit library except for a trivial rescaling of the velocities.

Table 1 presents the properties of the galaxies in this sample. The columns are (1) galaxy name, (2) galaxy type, (3) absolute B-band bulge luminosity, (4) BH mass and its 68% uncertainty, (5) effective velocity dispersion σ_e (which is defined in § 4.6), (6) distance in Mpc, (7) mass-to-light ratio and the band, (8) central slope of luminosity density, (9) shape of the velocity dispersion tensor in the central model bin, (10) shape of the velocity dispersion tensor at a quarter of the bulge half-light radius, and (11) half-light radius of the bulge. Bulge magnitudes come from Kormendy & Gebhardt (2001). The half-light radii come from Faber et al. (1989) and Baggett, Baggett, & Anderson (1998).

In all but two of the galaxies, there is little covariance between BH mass and M/L. The reason is that we are probing those regions where the BH mass dominates the potential with multiple resolution elements. Since the stars contribute a small fraction of the total mass in this region, varying their mass-to-light ratios has little effect on the enclosed mass. The two cases in which there is some covariance, NGC 3377 and NGC 5845, have high-resolution kinematic data from only a single FOS aperture. Thus, they have poorer spatial sampling inside of the region where the BH dominates the potential.

Figure 4 shows χ^2 as a function of BH mass for NGC 4564. This plot has been marginalized over M/L. For this galaxy, we have spectra at 33 spatial positions. With 13 velocity bins each, we then have 429 kinematic measurements. The velocity profiles have a smoothing width of about two bins, and thus the number of degrees of freedom is about 210. For NGC 4564, we ran a large number of models in order to inspect the shape of the χ^2 distribution and its asymptotic shape at small mass. Near the minimum of the χ^2, there is noise at the level of $\Delta\chi^2 \approx 0.5$.
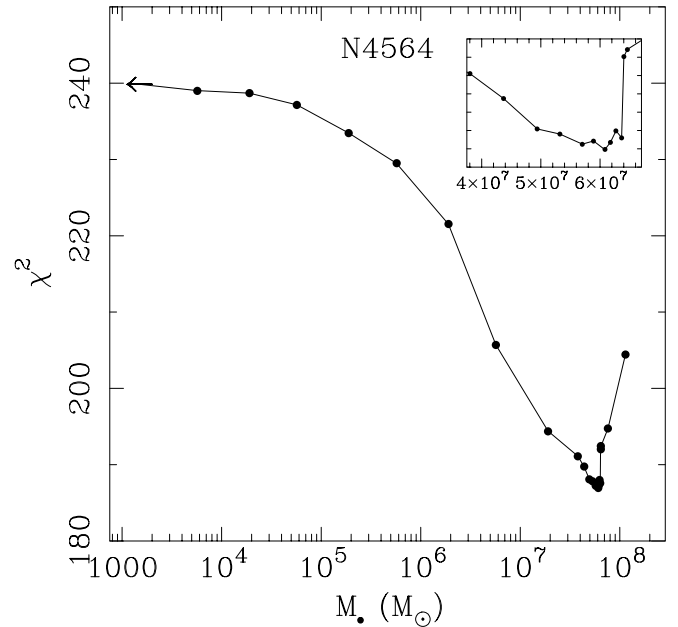

Fig. 4.—χ^2 as a function of BH mass for NGC 4564 marginalized over the mass-to-light ratio. The inset box is a magnified view of the region near the minimum. The tick marks along the ordinate on the inset represent $\Delta\chi^2 = 1$.

Figure 5 shows the χ^2 distributions for the whole sample of 12 galaxies. These plots have been marginalized over M/L, so χ^2 is a function of only one variable, M_{BH}. In these plots, $\Delta\chi^2 = 1$ corresponds to 1 σ uncertainty or 68%. Thus, the detection of a BH, or, strictly speaking, of a massive dark object, is very significant in most of these galaxies. The least significant detection is NGC 2778 where the difference in χ^2 is less than 10 between the best-fit BH mass and zero BH mass.

TABLE 1
GALAXY SAMPLE

Galaxy (1)	Type (2)	M_B Bulge (3)	M_{BH} (low, high) $(M_\odot)$ (4)	σ_e (km s^{-1}) (5)	Distance (Mpc) (6)	M/L, Band (7)	$[(d\log\nu)/(d\log r)]_0$ (8)	$(\sigma_r/\sigma_t)_0$ (9)	$(\sigma_r/\sigma_t)_{R_e/4}$ (10)	R_e (kpc) (11)
N821	E4	−20.41	3.7×10^7 (2.9, 6.1)	209	24.1	7.6, V	−1.4	0.37	0.88	5.32
N2778	E2	−18.59	1.4×10^7 (0.5, 2.2)	175	22.9	8.0, V	−1.9	0.56	0.81	1.82
N3377	E5	−19.05	1.0×10^8 (0.9, 1.9)	145	11.2	2.9, V	−1.5	0.74	1.01	1.82
N3384	S0	−18.99	1.6×10^7 (1.4, 1.7)	143	11.6	2.5, V	−1.9	0.44	0.89	0.73
N3608*	E2	−19.86	1.9×10^8 (1.3, 2.9)	182	22.9	3.7, V	−1.0	0.52	1.00	3.85
N4291*	E2	−19.63	3.1×10^8 (0.8, 3.9)	242	26.2	5.5, V	−0.6	0.42	0.98	1.85
N4473*	E5	−19.89	1.1×10^8 (0.3, 1.5)	190	15.7	6.0, V	−0.3	0.33	0.79	1.84
N4564	E3	−18.92	5.6×10^7 (4.8, 5.9)	162	15.0	2.0, I	−1.9	0.62	0.89	1.54
N4649*	E1	−21.30	2.0×10^9 (1.4, 2.4)	385	16.8	8.5, V	−1.2	0.51	1.04	5.95
N4697	E4	−20.24	1.7×10^8 (1.6, 1.9)	177	11.7	4.7, V	−1.7	0.97	0.92	4.25
N5845	E3	−18.72	2.4×10^8 (1.0, 2.8)	234	25.9	5.5, V	−1.4	0.79	1.07	0.51
N7457	S0	−17.69	3.5×10^6 (2.1, 4.6)	67	13.2	3.2, V	−1.9	0.62	0.72	0.90

NOTE.—An asterisk denotes a core galaxy; the others are power-law galaxies. The bulge, B-band magnitudes come from Kormendy & Gebhardt 2001; σ_e comes from the ground-based spectra integrating from $\pm R_e$ along the major axis with a 1″ slit. The BH mass offsets used in Fig. 9 represent the difference between the BH mass in this table and that mass using the correlation from Tremaine et al. 2002 with the σ_e reported in this table. The distances come from Tonry et al. 2000. The mass-to-light ratios come from the best fit for the dynamical models presented in this paper and generally have uncertainties smaller than 2%. The central radial to tangential dispersion ratios come from an average of the value in central bins along those position angles for which we have kinematic data (from one to three position angles; see Table 2). The ratio at $R_e/4$ is an average of the three bins nearest in radii to $R_e/4$ along the position angles that have kinematic data. R_e comes from either Faber et al. 1989 or Baggett et al. 1998.
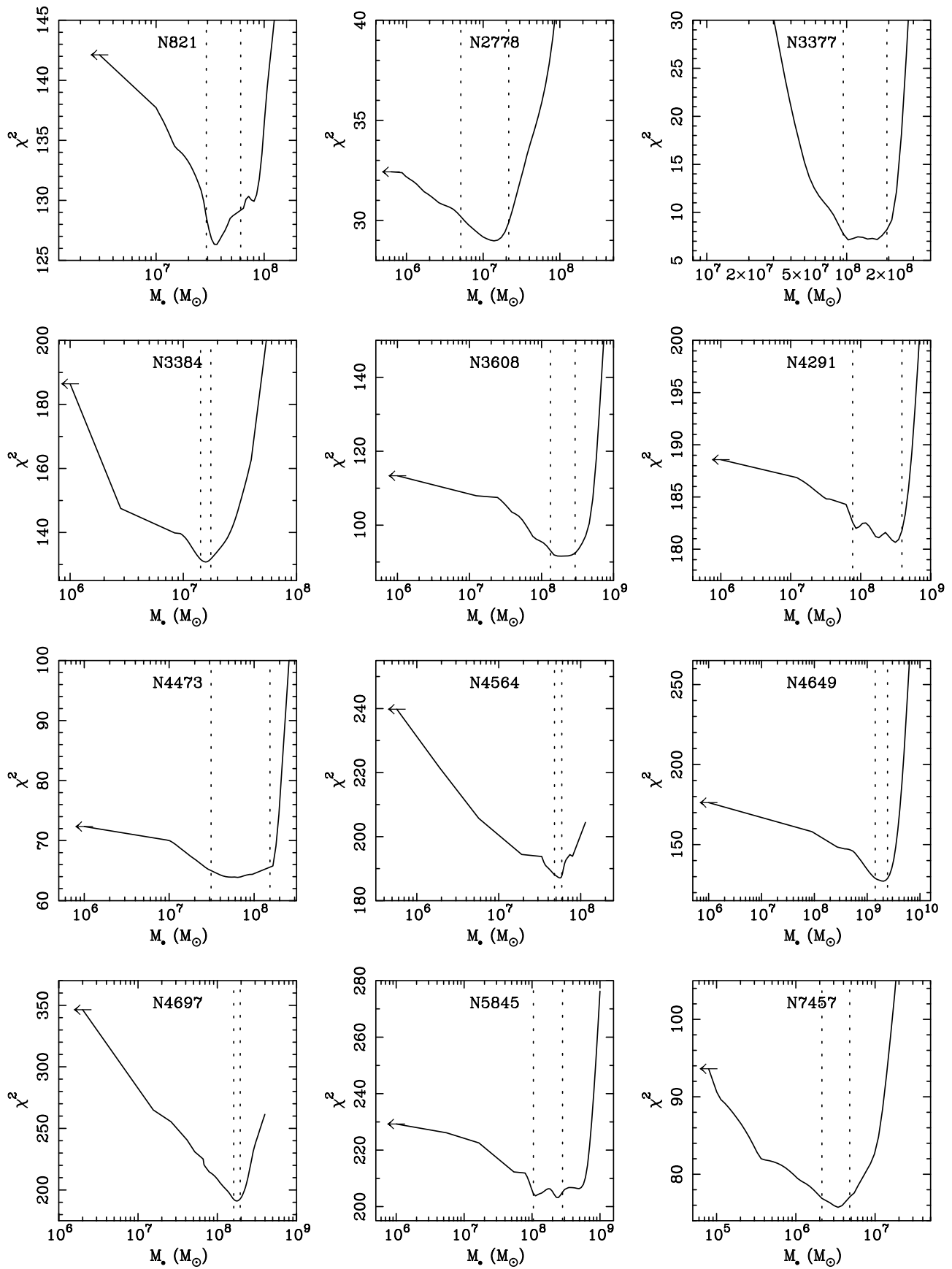
FIG. 5.—χ^2 as a function of BH mass for each of the galaxies. We have marginalized over the mass-to-light ratios. The vertical dashed lines are the 68% confidence bands quoted for the BH mass uncertainties. The arrow on the leftmost point indicates that this point is actually at zero BH mass, off the edge of the panel. [*See the electronic edition of the Journal for a color version of this figure.*]

We note the difference in the convention used here for the contour levels compared to other orbit-based studies. We report uncertainties that are based on 1 degree of freedom (i.e., marginalizing over the other parameters) and are at the 68% level (1 σ). Other studies have used different values. Van der Marel et al. (1998) report 3 σ uncertainties based on 2 degrees of freedom (BH mass and mass-to-light ratio) corresponding to $\Delta\chi^2 = 11.8$. Cretton & van den Bosch (1999) report 1 σ uncertainties with 2 degrees of freedom corresponding to $\Delta\chi^2 = 2.3$. Cappellari et al. (2002) and Verolme et al. (2002) report 3 σ uncertainties with 3 degrees of freedom (including inclination) corresponding to $\Delta\chi^2 = 14.2$. Our intention is to use the BH masses reported here in galaxy parameter studies, and so we desire a BH mass uncertainty that has been marginalized over all other parameters. Furthermore, convention suggests that 1 σ uncertainties are the most useful for parameter studies. Thus, we use 1 σ, 1 degree of freedom uncertainties. We also convert the uncertainties from the orbit-based studies above to our convention of $\Delta\chi^2 = 1.0$. The three galaxies for which we converted the uncertainties are M32 (Verolme et al. 2002), NGC 4342 (Cretton & van den Bosch 1999), and IC 1459 (Cappellari et al. 2002). In order to do this properly requires sampling the dynamical models finely enough to see $\Delta\chi^2 = 1.0$ variations. Since the above studies were not concerned with the uncertainties at this level, we must use an approximation. We can use the χ^2 contours from our sample to approximate the change in BH mass uncertainty relative to change in χ^2. This is not ideal but does serve as a first approximation. Thus, $\Delta\chi^2$ changing from 14.3 to 1.0 implies an average change in the BH mass uncertainty of a factor of 4 (which we use for M32 and IC 1459). Going from $\Delta\chi^2$ of 2.3 to 1.0 implies an uncertainty change of a factor of 1.6 (which we use for NGC 4342).

Most of the galaxies in our sample have significant flattenings. Since it appears that the distribution of intrinsic flattenings peaks at axis ratio 0.7 (Alam & Ryden 2002), most of our galaxies should not be far from edge-on. Except for NGC 4473, all of the models presented in Figure 5 assume edge-on configuration. We have run a few inclined models for NGC 3608 and NGC 5845. In both cases, the BH mass is within the uncertainty given for the edge-on model. For the more face-on configurations, the BH mass increased by 30% for NGC 3608 and decreased by 20% for NGC 5845. Gebhardt et al. (2000a) found that some inclined models for NGC 3379 had BH masses larger by a factor of 2 compared to the edge-on case (but still within the uncertainty). However, the data used for these studies have limited spatial kinematic coverage. The two-dimensional kinematic data set used for M32 (Verolme et al. 2002) provides the optimal way to study inclination effects. They find that the more face-on case gives a 30% decrease in the BH mass measured from the edge-on model. Since we do not have adequate angular kinematic data to constrain the inclination, we rely on the above studies and the few cases that we have run to determine the inclination effect. On average, it appears that inclination will cause a 30% random change in the BH mass. Our BH mass uncertainties range from 10% to 70%, with the most flattened, nearly edge-on, galaxies tending to have the smallest uncertainties. For those galaxies where inclination might be a concern, their uncertainties are larger than 30%. Thus, we do not include any additional uncertainty that might be caused from using the incorrect inclination. The uncertainties given in Table 1

include those as measured from the edge-on models alone (or from the one inclined case for NGC 4473). Inclined models do, however, affect the M/L; as the galaxy approaches a more face-on configuration, it becomes more intrinsically flat in order to give the same projected flattening. Since it must maintain a similar projected dispersion, the smaller column depth for the more flattened galaxy requires a higher M/L, which is what is seen in the models.

The uncertainty in the BH mass determination clearly depends on both the spatial resolution and the S/N of the data. The spatial resolution can be parameterized relative to the radius of the sphere of influence, GM_{BH}/σ^2. For our galaxies, these radii range from $0\rlap{.}''02$ in NGC 2778 to $0\rlap{.}''75$ in NGC 4649. The size of the central bin used in the modeling is $0\rlap{.}''05$. Thus, for NGC 2778, the sphere of influence is more than a factor of 2 below our resolution limit. Because of this small radius, we have tried a variety of different data sets applied to the NGC 2778 models and find similar results. The zero BH mass model for NGC 2778 is ruled out at only the 95% confidence limit—our least confident detection. For all other galaxies, the sphere of influence is larger or equal to our resolution limit.

The uncertainties in the BH mass come from the shape of the one-dimensional χ^2 contours. It is important to check whether this estimate of the uncertainties properly reflects the true uncertainties. We can check this to a limited extent through Monte Carlo simulations of the kinematics. We note that this study will only determine the uncertainties within our assumptions; we discuss effects from relaxing our assumptions in § 4.9. We use the same Monte Carlo realizations that were used for the spectra (as described in Pinkney et al. 2002). For each realization of the set of LOSVDs we find the BH mass that provides the minimum χ^2. With 100 realizations, we then determine the 68% confidence limits from the Monte Carlo and compare that to the same limits as determined from the shape of the χ^2 contour. The uncertainties as measured from both techniques are in excellent agreement. Assuming that the Monte Carlo simulations should provide the most accurate uncertainties, we find no reason to question the uncertainties as measured from the χ^2 shape, as a result of their concordance. We have run this experiment only on NGC 3608 but believe these results to be general.

Gebhardt et al. (2000b) presented preliminary BH masses based on this analysis. Most of the preliminary masses are the same as those presented here, except for changes due to the change in assumed distance ($M_{BH} \propto$ distance). The few other differences arise because we now use a higher resolution grid of models, so the minimum of χ^2 is located more accurately. The changes in both the best-fit mass and the uncertainties are generally less than 0.5 σ. The most extreme change is in NGC 5845 since the lower limit for that galaxy was defined using a very poorly sampled grid.

4.2. *Individual Galaxies*

Pinkney et al. (2002) provide observational notes for the 10 galaxies in our sample that were observed with STIS. Here we report any additional details of the dynamical models for our sample of 12 galaxies. In addition, we include notes for five other galaxies taken from the literature that have similar models and are used in the analysis in §§ 4.5 and 4.7.

TABLE 2

MODEL PARAMETERS

Galaxy (1)	M_{BH} (low, high) (all data) ($M_\odot$) (2)	M_{BH} (low, high) (ground only) ($M_\odot$) (3)	$N_{P.A.}$ (HST, ground) (4)	N_{Pos} (5)	N_{Fit} (6)	χ^2 Minimum (7)
N821	3.7×10^7 (2.9, 6.1)	3.0×10^7 (0.0, 8.0)	2 (1, 2)	24	312	128
N2778	1.4×10^7 (0.5, 2.2)	0.0×10^7 (0.0, 6.0)	1 (1, 1)	12	93	29
N3377	1.0×10^8 (0.9, 1.9)	1.2×10^8 (0.5, 2.0)	2 (1, 2)	15	52	8
N3384	1.6×10^7 (1.4, 1.7)	1.4×10^7 (1.1, 3.0)	2 (1, 2)	24	312	131
N3608	1.9×10^8 (1.3, 2.9)	1.4×10^8 (0.7, 3.0)	2 (1, 2)	24	312	92
N4291	3.1×10^8 (0.8, 3.9)	2.0×10^8 (0.0, 5.0)	3 (1, 3)	27	351	182
N4473	1.1×10^8 (0.3, 1.5)	2.0×10^7 (1.0, 9.9)	2 (1, 2)	24	312	64
N4564	5.6×10^7 (4.8, 5.9)	1.0×10^7 (0.6, 5.5)	3 (1, 3)	33	429	187
N4649	2.0×10^9 (1.4, 2.4)	1.5×10^9 (0.7, 2.5)	3 (1, 3)	35	455	128
N4697	1.7×10^8 (1.6, 1.9)	2.5×10^8 (1.6, 3.1)	3 (1, 3)	30	390	192
N5845	2.4×10^8 (1.0, 2.8)	3.0×10^8 (0.4, 4.5)	3 (1, 3)	25	325	205
N7457	3.5×10^6 (2.1, 4.6)	3.1×10^6 (0.0, 9.9)	3 (1, 3)	20	260	76

NOTE.—The BH masses come from fitting to all of the data (col. [2]) and fitting only to the ground-based spectral data (col. [3]). $N_{P.A.}$ (col. [4]) is the number of kinematic position angles, with the number of HST and ground-based position angles given in parentheses. N_{Pos} (col. [5]) is the total number of positions on the sky with kinematics (this includes both ground-based and HST data). N_{Fit} (col. [6]) is the number of kinematic data points used in the fits; for most galaxies we use 13 velocity bins to represent the LOSVD.

NGC 821.—There are 312 velocity constraints, coming from 24 spatial positions each with 13 LOSVD bins. Given that two to three adjacent bins are correlated from the velocity profile smoothing, the number of degrees of freedom is about 100, so the minimum χ^2 of 128 (Table 2) indicates a good fit.

NGC 2778.—There are additional ground-based data from Fisher, Illingworth, & Franx (1995) along the major axis. NGC 2778 is important because its BH mass is low relative to the M_{BH}/σ relation. We have modeled NGC 2778 using three ground-based data sets: the STIS data plus our ground-based data, the STIS data plus the Fisher et al. (1995) data, and the STIS data plus both ground-based data sets. All three best-fit BH masses are consistent at the 68% confidence level. The data from Fisher et al. (1995) have higher S/N, and so the results we present are based on the STIS data plus the Fisher et al. (1995) data.

NGC 3377.—The BH mass in NGC 3377 was first measured in Kormendy et al. (1998) using only ground-based data; the mass that we find here is within their uncertainties. We use ground-based data from Kormendy et al. (1998) along the major and minor axes. Kormendy et al. (1998) present only the first two moments of the velocity distribution. Since our models require data on the full LOSVD, we convert these moments into a Gaussian velocity profile. The uncertainties are generated through a Monte Carlo procedure; we generate 1000 velocity profiles consistent with the means and uncertainties of the moments. The uncertainty at each velocity bin is given from the 68% range about the mean in the simulations. From HST, we have two FOS observations, which we present in the Appendix. Since we only use the first two moments for the ground-based data to generate the LOSVD and since galaxies can have significantly non-Gaussian LOSVDs, we have checked whether including additional moments affects the results. We have included a variety of H3 and H4 components for the ground-based data, using values that are consistent with those from other galaxies. We find little difference in the BH

mass as reported in Table 1. The main reason for this is that the HST data show a dramatic increase in the central dispersion and in the rotation relative to the ground-based data. Thus, the BH mass is determined mainly from the radial change in the kinematics and not from the higher order moments of the LOSVD.

NGC 3384.—NGC 3384 is one of the two galaxies that show a smaller velocity dispersion in the HST data than in the ground-based data. The reason for this drop is that the STIS kinematics is coming mainly from a cold edge-on disk. The dynamical models are free to include as many circular, or nearly circular, orbits as necessary, and so they easily match the kinematic profile. NGC 3384 is one of the more significant BH detections.

NGC 4473.—NGC 4473 shows a flattening in the central isophotes and also a significant decrease in the central dispersion. Both of these indicate the presence of a central disk (see Pinkney et al. 2002). Central stellar disks are seen in many elliptical galaxies (Jaffe et al. 1994; Lauer et al. 2002). In order to provide the best representation for the dynamical models, we include a central disk. The parameters of the disk are measured from the HST images. We use a spheroidal representation for the bulge component and model the residual with a zero-thickness disk with an exponent of 0.5. The parameters for the exponential disk are 4.9×10^7 $L_\odot$ arcsec^{-2} for the central surface brightness and $1''.0$ for the scale length. The best-fit inclination is $72°$, which we also assume for the galaxy. The mass of the disk inside of $1''$ is 20% higher than the bulge mass in that region. Thus, it does have a noticeable effect on the kinematics. The models have no problem matching the high rotation and low dispersion of the disk.

NGC 4649.—NGC 4649 is the largest galaxy in our sample and has the lowest surface brightness. We spent 22 HST orbits exposing on this galaxy. The central dispersion, 550 km s^{-1}, is the highest ever observed. Despite the large dispersion and low surface brightness, both of which strongly affect the S/N, the uncertainty in the BH mass is only 30%.

NGC 4697.—There is a gas disk in the center of this galaxy, and the gas kinematics for this galaxy is measured by J. Pinkney et al. (2003, in preparation). NGC 4697 has the most significant BH detection. The difference in χ^2 between the zero BH mass model and the best-fit model is 155.

NGC 7457.—There is a central point nucleus in NGC 7457. When measuring the surface brightness profile, we first subtract a point source from the center. Thus, for the stellar luminosity density, we assume that the point source is coming from nonthermal emission and does not contribute to the stellar density. If the point source is a nuclear star cluster instead of weak nuclear activity, then we will bias our BH mass since we would have then ignored some of the stellar mass. The total light in the point source is substantial, $V \approx 18.1$ mag. This amount of light translates into 1×10^7 $L_\odot$. Given the BH mass that we measure of 3.5×10^6 $M_\odot$, assuming that the point source is stellar is inconsistent with the STIS kinematics. The other effect that it may have is in the kinematics since the radius at which the point source is contributing light may be much smaller than the STIS pixels. Thus, the smaller radius would imply a smaller BH mass for the same dispersion measure. We do not have a good way to estimate this effect since it would depend strongly on the actual size of the assumed point source, but we can get some feel by comparing results from models using only ground-based observations. For those data, we measure a BH mass similar to that when including the STIS data, suggesting that the point source does not have a dramatic effect on the kinematics.

There are two main observations that suggest that the point source is nonthermal. First, the STIS kinematics show a significant decrease in the equivalent widths of the Ca II triplet lines. The drop is around 40%, suggesting nearly equal contribution from stellar and continuum sources. This drop is also seen in the ground-based data, which had a spatial FWHM of ∼1″. Second, the point source is unresolved at *HST* resolution. At 13.2 Mpc, the implied scale for the source is less than 2 pc. Given the luminosity of the source, this radial scale implies an extremely dense structure, denser than any known stellar cluster. These two facts lead us to conclude that the source is nonthermal and must be excluded from the dynamical analysis. The most likely explanation is that the point source is a weak AGN. Ravindranath et al. (2001) find nuclear sources in 40% of galaxies that they observed with *HST*, and they conclude that most of these are likely weak AGNs. Ho, Filippenko, & Sargent (1995) see no obvious nuclear emission from NGC 7457, and we conclude that it is most likely a weak BL Lac object. The luminosity density for NGC 7457 in Figure 1 excludes the central point source.

Below are notes for the other galaxies with orbit superposition models taken from the literature.

M32.—Verolme et al. (2002) have used both STIS spectroscopy and high-S/N ground-based two-dimensional spectra to provide one of the best measured BH masses using orbit-based models.

NGC 1023.—The results for NGC 1023 are given by Bower et al. (2001) and will not be repeated here. The only difference is the assumed distance, which changes both the BH mass ($M_{\rm BH} \propto$ distance) and the mass-to-light ratio ($M/L \propto 1/$distance).

NGC 3379.—The data and orbit superposition models are presented by Gebhardt et al. (2000a). NGC 3379 has only a single FOS pointing using the 0″21 aperture.

NGC 4342.—Cretton & van den Bosch (1999) use seven FOS aperture pointings and ground-based data along several position angles. The FOS aperture had 0″26 diameter.

IC 1459.—Cappellari et al. (2002) use both STIS spectra and extensive two-dimensional ground-based spectral coverage. This galaxy is very important since it also has a measurement of the BH mass from gas kinematics (Verdoes Kleijn et al. 2000). The stellar kinematic measurement is almost a factor of 6 higher than the gas measurement. This discrepancy is far larger than the typical error from our sample measured from stellar kinematics. However, important uncertainties attach to gas measurements, such as the orientation of the innermost gas disk and the assumption that the gas is in perfectly circular orbits. The large residual here suggests that these uncertainties perhaps deserve more attention than they have received to date.

4.3. *Quality of the Fit*

Figure 6 presents the rms line-of-sight velocity as a function of radius for both the data and best-fit model. [Strictly, we show $(V^2 + \sigma^2)^{1/2}$, where V and σ are the mean velocity and dispersion of the Gaussian that appear in the Gauss-Hermite expansion of the LOSVD.] We stress that the model uses the velocity profiles in the fitting and not the second moments directly. Thus, there are more parameters that control the quality of the fit than those shown in Figure 6. In addition, some galaxies have several position angles, and we show only one in Figure 6.

For each galaxy, the solid red line and the dashed blue line come from the same model; the only difference is that they use a different PSF. For example, the central ground-based measurements for NGC 3377, NGC 3608, NGC 4564, and NGC 7457 are all significantly different from the central STIS measurement. This is due to the smaller PSF of *HST*, which is taken into account in the model. There are two galaxies, NGC 821 and NGC 4564, which show a spike in the second moment at the outer STIS radius. This spike is an artifact since we are using only V and σ from the Gauss-Hermite fits, as opposed to including the higher order moments, H3 and H4, in the estimate of the second moment.

In order to judge the quality of the fit, we have to compare χ^2 to the number of degrees of freedom (ndof). The ndof is difficult to measure mainly because there is a smoothing parameter in the estimation of the velocity profiles; this effect typically decreases the ndof by a factor of 2. An additional difficulty in calculating the ndof arises since we often include the outer regions of the velocity profiles where they have no light in the models. Sometimes these regions extend to velocities that are either outside of those measured in the velocity profiles or very uncertain there. In the regions that are beyond the velocities in which the LOSVDs probe, we use the uncertainty at the last measured velocity. Since we have no velocity profile there, we also set the observed LOSVDs in those bins to zero. Thus, the result is to add zero to the overall χ^2, yet increase the ndof. The problem can most easily be seen in a galaxy that has a significant dispersion gradient with radius. For the modeling, we use a fixed velocity interval and bins for the LOSVD. In such a galaxy with a large dispersion gradient, the outer edges of the velocity profile in the center of the galaxy will contain some light, while those regions at large radii will not. This effect can be dramatic in some galaxies, causing about half of the velocity
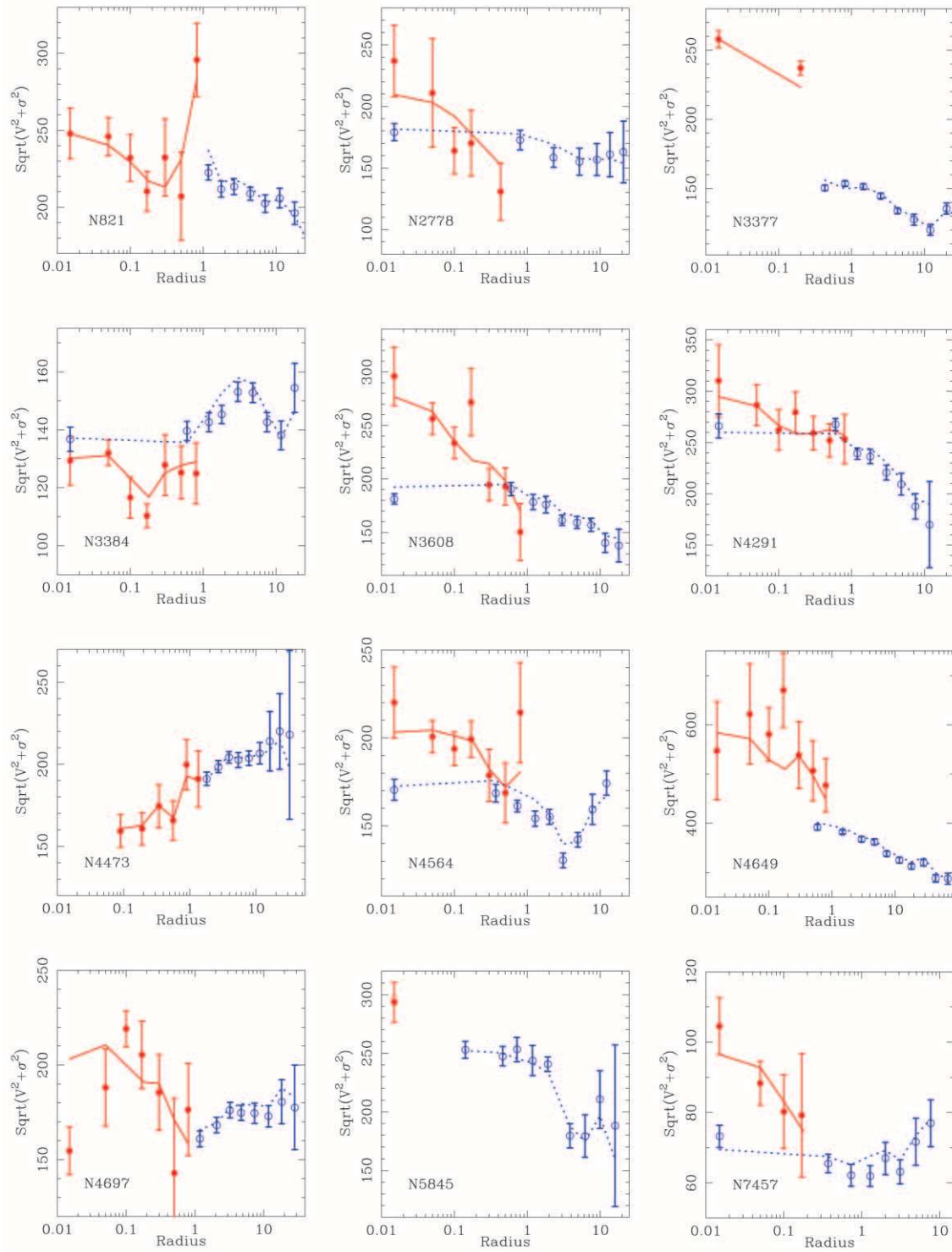
FIG. 6.—The rms line-of-sight velocity $(V^2 + \sigma^2)^{1/2}$ (in km s^{-1}) as a function of radius (in arcseconds) for each of the galaxies along the major axis. We use V and σ as measured from a Gauss-Hermite fit; since we do not correct for the higher order moments, these values approximate the actual second moment. The red filled circles are the *HST* (STIS or FOS) measurements, and the blue open circles are the ground-based values. The lines are the model results: red solid lines include the *HST* PSF, and the blue dotted lines include the ground-based PSF. For NGC 5845, the model value for the central FOS measurement is shown as an open square. We provide these plots only for comparison and note that the models minimize χ^2 using the full LOSVD rather than its second moment.

bins to have zero light for the large-radii LOSVD. Thus, there is a further reduction in the ndof that one needs to apply in order to judge the quality of the fit. Column (6) in Table 2 reports the total numbers of fitted parameters for each of the galaxies. Comparing these numbers to the total

minimum χ^2 (col. [7], Table 2) shows that the χ^2 values are about 2–3 times lower than the ndof, implying reduced χ^2 values near 0.4. However, this low reduced χ^2 is in good agreement with the reduction expected from the two effects above.

4.4. *The Need for HST*

The high-resolution spectral data presented here represent over 100 orbits of *HST* time. It is illuminating to determine the importance of these observations compared to ground-based data. For each galaxy, we have recomputed the best-fit models using *only* the ground-based spectra (we still use both ground-based and *HST* photometry). Figure 7 plots the χ^2 as a function of BH mass for both sets of data (the *HST* plus ground and ground only). In every case, inclusion of the *HST* data makes a substantial improvement in the significance of the BH detection (see also Table 2).

The two galaxies with the strongest BH detection based on the ground-based data are NGC 4649 and NGC 4697. Of the 12 galaxies in the sample, these two have the largest angular sphere of influence, $0\rlap{.}{''}75$ and $0\rlap{.}{''}4$, respectively. The ground-based data come from MDM where the seeing is typically $1''$. Thus, it is not too surprising that we can detect the BH in these galaxies without *HST* data. However, when the *HST* data are included, in both of these galaxies the significance is greatly increased.

We can also check whether the BH masses estimated from the two sets of data are the same. Figure 8 plots this comparison. All of the masses estimated from the two sets of data are consistent at the $1\,\sigma$ level (i.e., all of the error bars in Fig. 8 overlap the straight line). There is no evidence that masses based on ground-based data alone are systematically high; if anything, the use of ground-based data alone appears to slightly *underestimate* the BH mass. A striking feature of Figure 8 is that even when the $1\,\sigma$ uncertainty in the BH mass from ground-based data includes zero, the best-fit mass from these data is very similar to the best-fit mass from the full data set.

Magorrian et al. (1998) presented masses based on ground-based data and two-integral axisymmetric models. Subsequent analysis shows that some of the BH masses were overestimated by up to a factor of 3. Merritt & Ferrarese (2001) argue that this bias is due to the use of ground-based data. From the results presented here, it appears that the problem does not lie in using ground-based data, but more likely in the model assumptions. For the eight galaxies common to the present paper and Magorrian et al. (1998), we find that using our higher resolution *HST* plus MDM kinematics has little effect on the BH masses found by the two-integral models. Therefore, the error in the BH masses of Magorrian et al. (1998) is due to their assumption of isotropy. In particular, the axisymmetric models in this paper exhibit some radial anisotropy in the velocity dispersion tensor at midrange radii; as Magorrian et al. (1998) point out, radial anisotropy will cause the simpler isotropic models used in that paper to overestimate the masses. For the 12 galaxies in Magorrian et al. (1998) that have nonzero BH mass estimates and are also in the Tremaine et al. (2002) sample, the mean overestimate in $\log M$ is 0.22 dex.

We have also investigated whether reliable BH masses can be obtained from *HST* spectral data alone, excluding the ground-based spectra. We ran the models on the one galaxy that should have produced the strongest BH detection based on *HST* alone. NGC 3608 shows a dispersion increase by a factor of 2 just in the *HST* data, from $0''$ to $1''$. For these data, we find *no* significant detection for a BH, suggesting that the ground-based data are necessary to measure one. The reason is that the stellar M/L is unconstrained by the *HST* data alone. The M/L implied for NGC 3608 from the *HST* data is about a factor of 2 higher than that found when using all of the data together. This increase in the M/L causes the significance of the BH detection to disappear in the *HST* data alone.

4.5. *Black Hole Correlations with Galaxy Properties*

We are now in a position to compare BH masses with other host galaxy properties, to look for underlying relationships that may inform us about the formation process of the BH. In Figure 9, we plot 10 galaxy properties, including the BH mass, against one another. For example, in the first plot on the left on the top row, we plot the BH mass along the abscissa and the bulge luminosity along the ordinate. In addition to the galaxies with BH masses measured in this paper, we have added other galaxies with reliable mass estimates, for a total sample of 31 galaxies. Tremaine et al. (2002) report some of the properties of the galaxies not included here. In Figure 9, the number of galaxies in each panel changes depending on whether that particular value exists for all 31 galaxies. However, we do differentiate between those galaxies studied with orbit-based models (*filled symbols*) and those with other models (*open symbols*).

The galaxy properties that we report are bulge luminosity, BH mass, effective dispersion (discussed below), radial to tangential dispersion at the galaxy center (discussed below), mass-to-light ratio in the V band, bulge half-light radius R_e, central luminosity density slope ($d \log \nu / d \log r$, where ν is the luminosity density), radial to tangential dispersion on the major axis at a quarter of the half-light radius, bulge stellar mass, and BH mass offset from the M_{BH}/σ correlation. The bulge luminosities are taken from Kormendy & Gebhardt (2001), and the calculations are given by Kormendy et al. (2002). The bulge half-light radii come from Faber et al. (1989) and Baggett et al. (1998). The BH mass offset is calculated using the relation in Tremaine et al. (2002). For the mass-to-light ratios, we use only those galaxies that have a measured value in the V band. To measure the total mass, we use the bulge total B-band light, convert to V using $B-V$ from RC3 (de Vaucouleurs et al. 1991), and multiply by the V-band mass-to-light ratio.

There are five galaxies that have axisymmetric orbit-based models from previous studies. We include the internal velocity structure of these five galaxies in Figure 9 and subsequent analysis. Table 3 reports their internal velocity moments and the reference.

Besides the obvious and expected correlation between total mass and total light, the most significant correlation is the M_{BH}/σ relation reported by Gebhardt et al. (2000b) and Ferrarese & Merritt (2000). Tremaine et al. (2002) discuss the differences in the measured slope of this relation. Most other significant correlations between various galaxy properties and the BH mass can be regarded as a result of well-known correlations of other galaxy properties with dispersion. There is a significant correlation between the shape of the dispersion tensor at $R_e/4$ and the BH mass. Larger BHs tend to live in galaxies that have more radial motion. This trend may be a clue to the formation process of the BH but also could represent a secondary correlation between galaxy anisotropy and galaxy dispersion. There is a suggestion that larger BH mass offsets occur in galaxies that have less radial energy near the center, possibly signifying additional evolutionary effects. However, we need more data to decide on the significance, since it is only at the 20% level in the aniso-
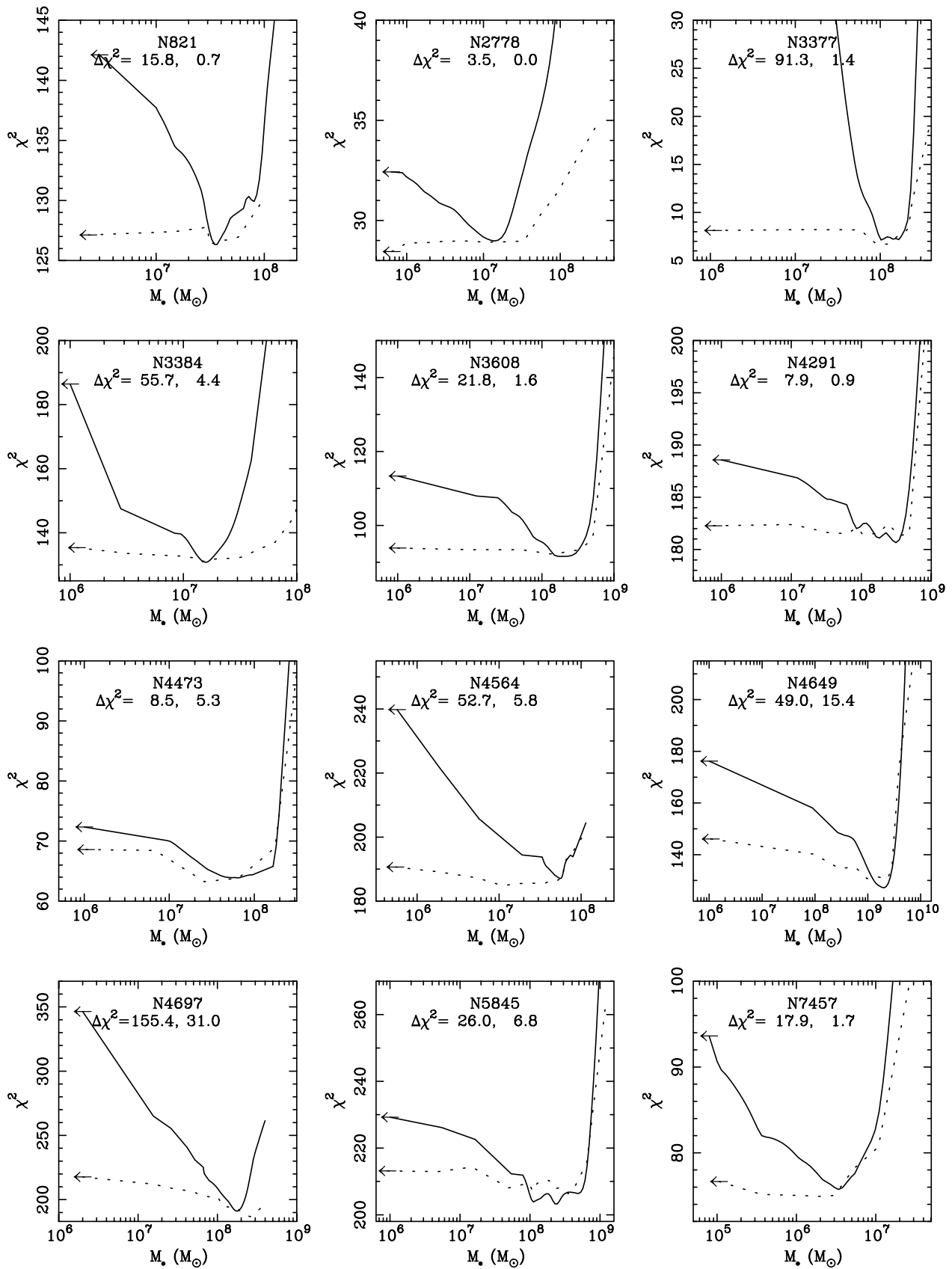
Fig. 7.—χ^2 as a function of BH mass using two sets of spectral data for each galaxy. The solid lines are the same as in Fig. 5, where we have included all of the spectral data (i.e., both *HST* and ground-based observations). The lower curves are the results when only including the ground-based spectral data, excluding the *HST* spectra; an offset has been added to the ground-based χ^2 values in order to compare better with the solid lines. Below the galaxy name, we have included the change in χ^2 between the zero BH model and the best-fit BH model, for both *HST* plus ground-based spectroscopy (*first entry*) and only ground-based spectral data (*second entry*). In every case, the significance of the BH detection is greatly enhanced by including the *HST* spectral data. [*See the electronic edition of the Journal for a color version of this figure.*]
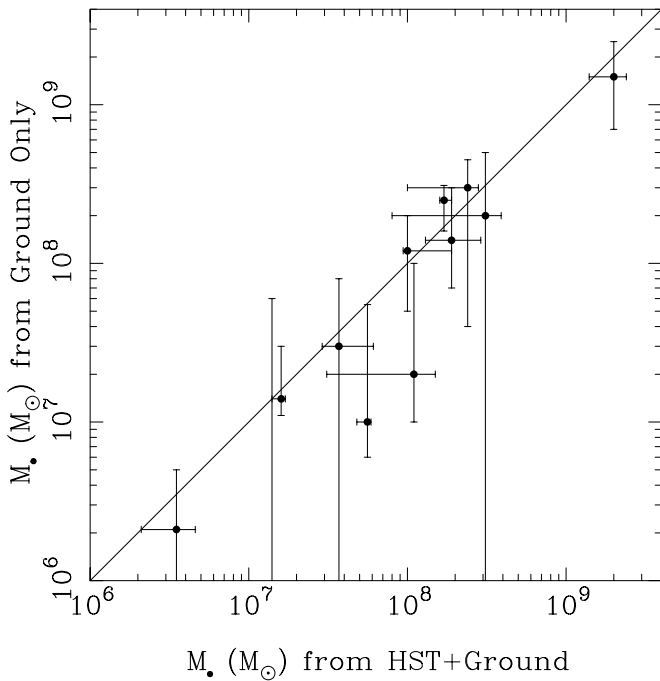
FIG. 8.—BH masses measured from all of the spectral data (*HST* and ground-based) compared to those measured from using the ground-based spectral data only. The confidence bands are 68% uncertainties. All measurements based on ground-based data alone are consistent with measurements based on *HST* plus ground-based data. The masses from the ground-based spectral data may tend to slightly underestimate those obtained including the *HST* spectral data.

the BH can have on either the effective dispersion or the dispersion inside $R_e/8$. In most cases, the BH has little effect, less than 3%, but in some galaxies the effect can be as large as 30%.

The effective dispersions are given in Table 1. In all cases the S/N is very high, over 100. The corresponding statistical uncertainty in σ_e ranges from 1% to 3%. However, at this level, systematic uncertainties dominate, particularly continuum estimation and template mismatch. We have investigated both of these effects by varying the continuum level and using different templates. We find that at any S/N, using an appropriate range of systematic variables, the overall uncertainty is no better than 5%. Therefore, we adopt 5% accuracy for the effective dispersion measurements. We discuss below how this choice affects the main results.

4.7. Velocity Dispersion Tensor

We show the shape of the velocity dispersion tensor in Figure 10. We define the tangential dispersion as $\sigma_t = [(\sigma_\theta^2 + \sigma_\phi^2)/2]^{1/2}$, so that for an isotropic distribution the radial and tangential dispersions are equal. Note that σ_ϕ includes both random and ordered motion (i.e., it represents the second moment of the azimuthal velocity relative to the systemic velocity, not relative to the mean rotation speed). The most obvious trend in Figure 10 is that the tangential motion tends to become more important toward the center (discussed below) in all galaxies except for NGC 4697.

We use two methods to measure the uncertainties on these quantities. We have run Monte Carlo simulations for two galaxies, and for the remaining we use the simple alternative of using the smoothness in both the radial and angular profiles to estimate the uncertainties. For the Monte Carlo simulations we use the same realizations that are used to generate the LOSVD uncertainties (Pinkney et al. 2002) and to generate the BH mass uncertainties. For each set of LOSVD realizations, we find the best-fit model and examine the orbital structure. We have run these simulations on two galaxies: the core galaxy NGC 3608 and the power-law galaxy NGC 4564. Figure 11 plots the results. For the 100 realizations we estimate the 68% confidence bands by choosing the 16% and 84% values in the sorted internal moments at each radii. Figure 11 shows that the drop in the radial motion near the center is statistically significant for both galaxies. At the radii outside of our last measured kinematic measurements, the uncertainties become very large, as expected. We note that the radial profiles are not very smooth. The level of nonsmoothness is consistent with the measured uncertainties. This noise is likely a result of using

tropy. A full treatment of the correlations should include a proper principal component analysis (PCA); however, given the uncertainties and small sample, we are not in a position to explore PCA, especially since the $M_{\rm BH}/\sigma$ relation provides such small scatter already.

4.6. Effective Dispersion

We use the effective dispersion, σ_e, as a representation of the galaxy velocity dispersion; σ_e is the second moment of the velocity profile integrated from $-R_e$ to $+R_e$ along the major axis with a slit width of $1''$. The idea is to represent the galaxy by one dispersion estimate. There are many ways to do this; for example, Jørgensen, Franx, & Kjærgaard (1996), Faber et al. (1989), and the Sloan Survey (Bernardi et al. 2002) use the second moment inside a circular aperture of radius $R_e/8$. Tremaine et al. (2002) discuss the effect that

TABLE 3
GALAXIES FROM OTHER SOURCES

Galaxy	$M_{\rm BH}$ (low, high)	$[(d \log \nu)/(d \log r)]_0$	$(\sigma_r/\sigma_t)_0$	$(\sigma_r/\sigma_t)_{R_e/4}$	R_e (kpc)	Reference
N221=M32..............	2.5×10^6 (2.4, 2.6)	-1.6	1.01	0.72	0.15	1
N1023	4.4×10^7 (3.9, 4.9)	-1.8	0.57	1.04	1.98	2
N3379*	1.0×10^8 (0.5, 1.6)	-1.0	0.41	1.06	1.76	3
N4342	3.0×10^8 (2.4, 4.1)	-1.7	1.03	1.00	0.47	4
IC 1459	2.5×10^9 (2.4, 2.6)	-1.4	0.81	1.12	4.48	5

NOTE.—An asterisk denotes a core galaxy. The uncertainties on the BH masses are 68% for 1 degree of freedom. For M32, N4342, and IC 1459 we approximate these 1σ uncertainties from the authors' quoted uncertainties.

REFERENCES.—(1) Verolme et al. 2002. (2) Bower et al. 2001. (3) Gebhardt et al. 2000a. (4) Cretton & van den Bosch 1999. (5) Cappellari et al. 2002.
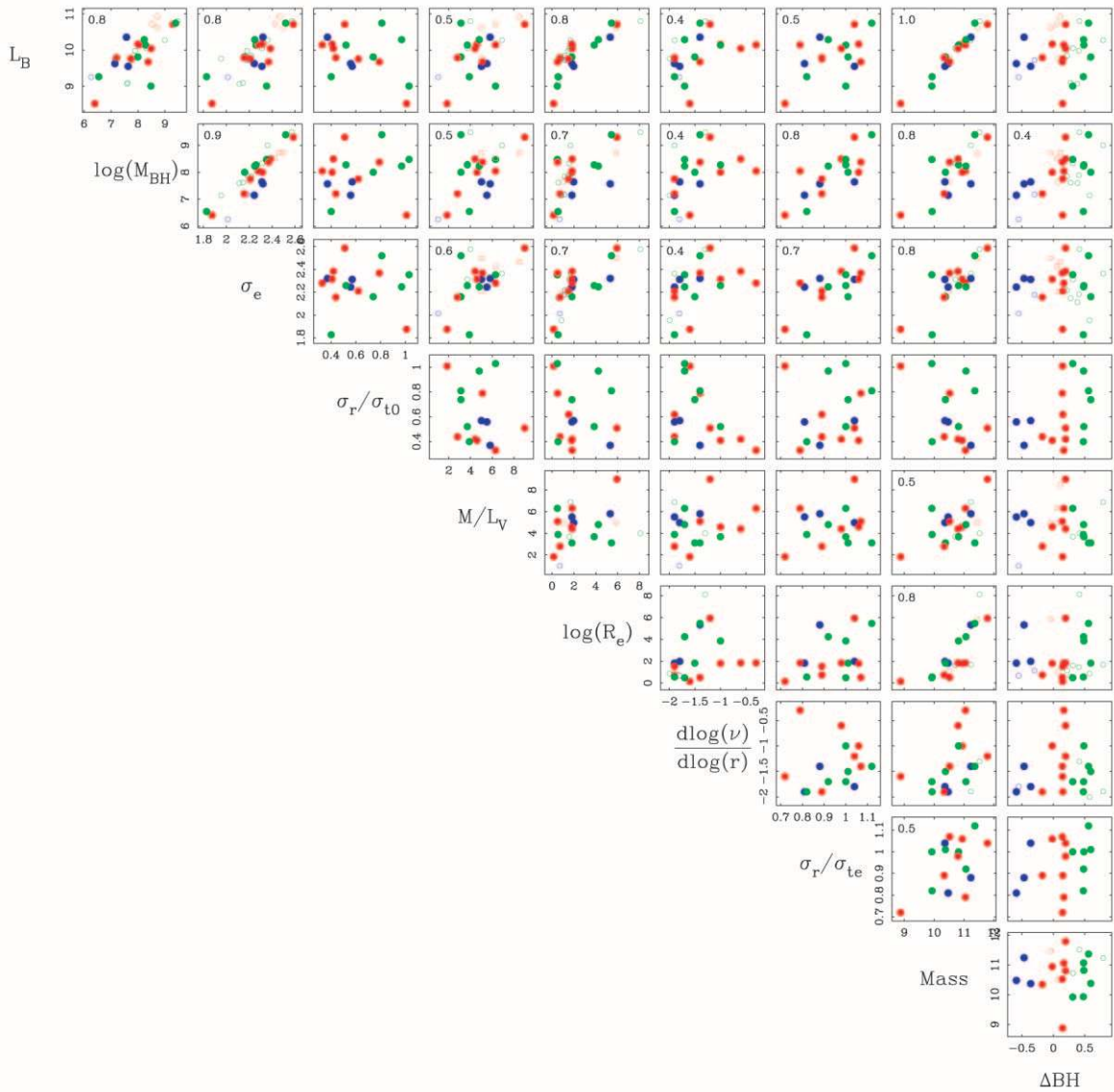
Fig. 9.—Ten galaxy properties plotted against each other, for the galaxies that have measured BH masses. For this plot, we include up to 31 galaxies; the BH masses are the same as in Tremaine et al. (2002). The colors represent the offset from the M_{BH}/σ correlation as defined in Tremaine et al. (2002), with green having the largest positive BH offset, blue having the largest negative offset, and red having small offset. The number written in the upper left-hand corner of the plot is the Pearson's R correlation coefficient. If the probability from the correlation is below 10%, we do not report R. Filled symbols are the 17 galaxies that have orbit-based models; the rest are plotted with open symbols.

the same orbit library with each new LOSVD realization. Thus, the remaining noise is due to using a limited number of stellar orbits. Ideally, we should include a random sampling of the photometry and hence the stellar potential in the Monte Carlo simulations. By doing so, we would average over noise from a particular set of orbits. However, this is computationally prohibitive, and we rely on the present simulations to provide the uncertainties.

For the other galaxies, we use deviations from smoothness as an estimate of the internal orbital structure uncertainties. An expectation is that the radial and angular gradient of the internal moments may be smooth, albeit details due to recent merger and accretion history may cause small-scale variations. Thus, deviations from a smooth profile may be indicative of the measurement uncertainty. The three galaxies with the smallest number of kinematic measurements, NGC 2778, NGC 3377, and NGC 7457, show the largest radial and angular variations, suggesting that these

are due to increased uncertainties from not having as many kinematic constraints. By inspection of variations seen in Figures 10 and 11, we estimate that the uncertainties on ratio of the internal moments is around 0.1–0.2 for most galaxies. This uncertainty is also consistent with the angular variations. The models are free to have very different dispersion ratios at different position angles and radii. The fact that the ratios are similar at different angles suggests that the measurements are robust for these models. The core galaxies (denoted with an asterisk) show a larger decrease in the ratio toward the center, which we discuss next.

Although the models produce the internal moments everywhere in the galaxies (i.e., Fig. 10), Figure 12 shows them only along the major axis and at two radii: the central bin in the models and an average of the three bins nearest $R_e/4$. The BH dominates the potential in the central bin.

Figure 12 shows that galaxies with shallow central density profiles have orbits with strong tangential bias near
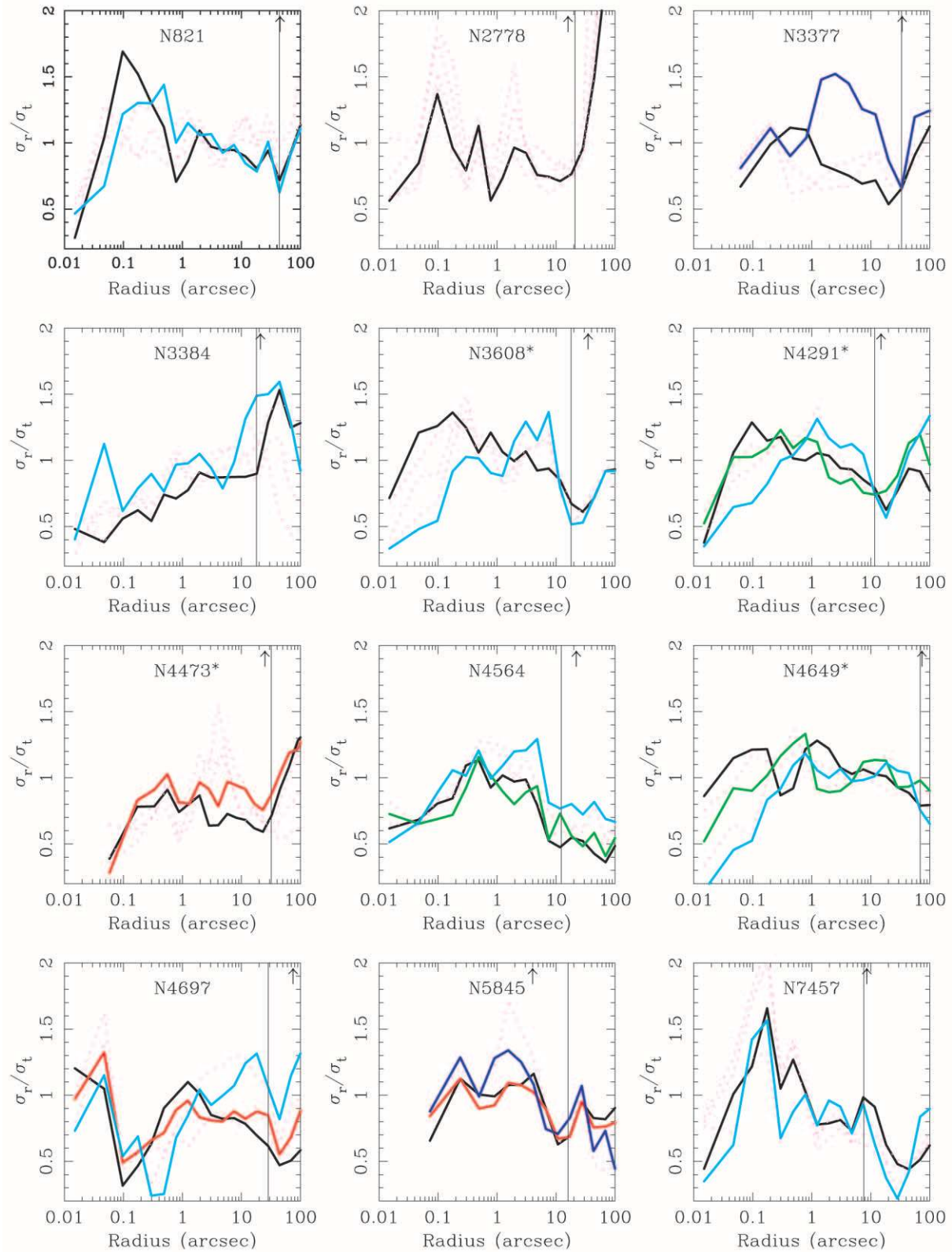
FIG. 10.—Shape of the velocity dispersion tensor for all 12 galaxies, plotted as a function of radius. The solid lines are at those position angles for which we have kinematic data. The dotted lines are those for which we do not have data but result from the maximum entropy solution for the best-fit model. The colors represent different position angles. The black line is along the major axis, and the light blue line is near the pole. Other colors are intermediate axes. The vertical solid line is the radial extent of the ground-based data, and the arrow is at the half-light radius. An asterisk denotes whether the galaxy is a core galaxy.

their centers. At larger radii, the orbits tend to be isotropic or slightly radial. There is a concern that this change in dispersion ratio may simply reflect our assumption that the mass-to-light ratio is independent of radius.

If a dark halo were present, so that the mass-to-light ratio increased outward, a galaxy with isotropic orbits will appear to become tangentially anisotropic at large radii. However, it is unlikely that the dark halo makes a
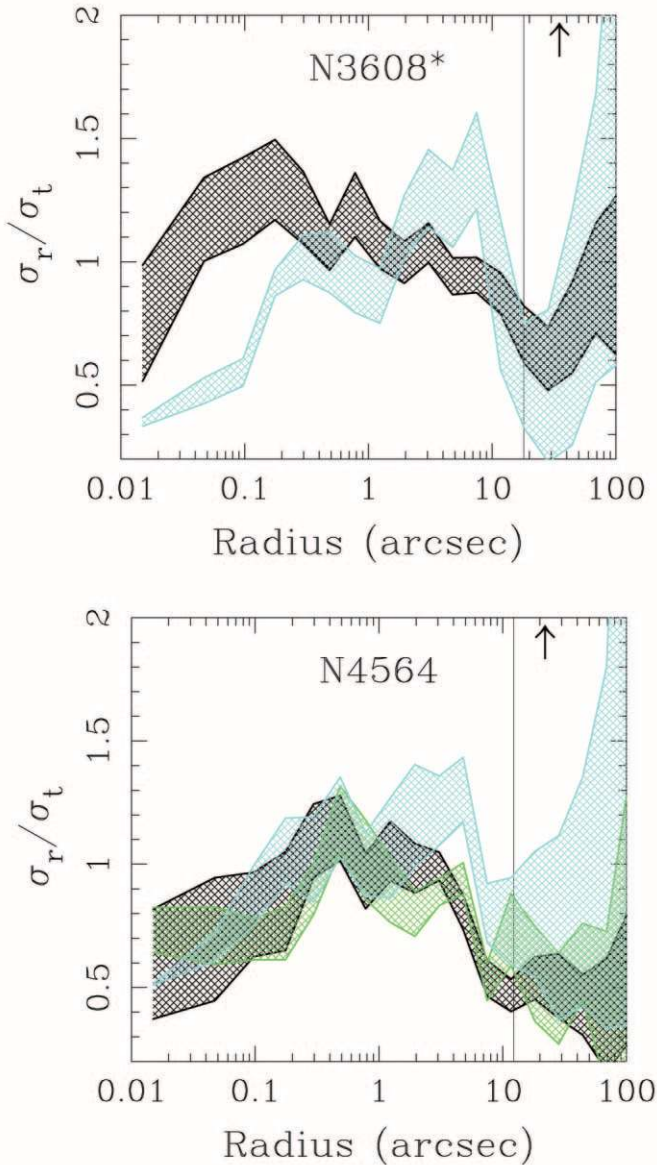
FIG. 11.—Same as Fig. 10, except here we include the 68% confidence bands based on Monte Carlo simulations for two of the galaxies. The colors refer to different position angles, as in Fig. 10. The colored hatched regions refer to their 68% confidence bands. The average uncertainty is around 0.15 in σ_r/σ_t. Beyond the region where we have no kinematic data (*vertical solid line*), the uncertainties increase dramatically.
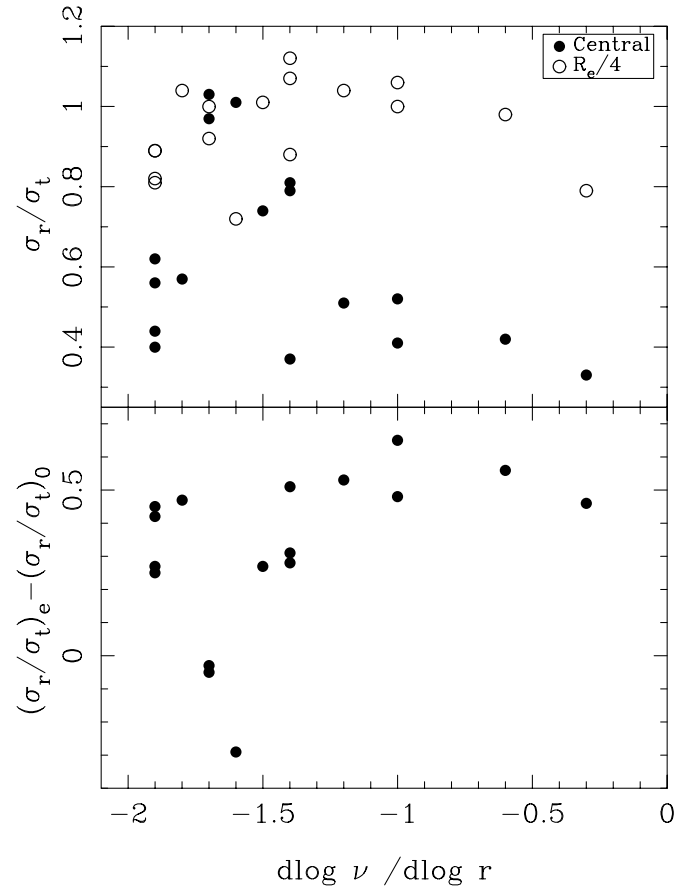

FIG. 12.—*Top*: Ratio of radial to tangential rms velocity, plotted as a function of central luminosity density slope. Each galaxy appears twice in the plot: the open symbols represent the ratio at $R_e/4$, while the filled symbols are the ratio in the central bin. An isotropic dispersion tensor corresponds to $\sigma_r/\sigma_t = 1$. In addition to the 12 galaxies in this paper, we include an additional five presented in Table 3. The division between core and power-law galaxies is around $d \log \nu/d \log r = -1.3$, with core galaxies having flatter profiles. *Bottom*: Change in shape of the velocity dispersion tensor (ratio of radial to tangential motion) from the center to $R_e/4$ as a function of central luminosity density slope. [*See the electronic edition of the Journal for a color version of this figure.*]

significant contribution to the potential within $R_e/4$, and in any case the sign of this trend (increasing tangential anisotropy with radius) is opposite to the one we observe. Figure 12 only includes results from radii that are small enough to be unaffected by the presence of a dark halo. In any event, the most likely bias is that, by not including a dark halo, we will overestimate the amount of tangential anisotropy at large radii. At small radii, the dark halo assumption will have no effect. Therefore, we are confident of the gradient seen in Figure 12.

The bottom panel in Figure 12 plots the change in the radial-to-tangential motion between the center and $R_e/4$ as a function of central slope. This plot reiterates that the gradient in shape of the dispersion tensor is larger for core galaxies than for power-law galaxies.

The shape of the velocity dispersion tensor depends on the galaxy formation process. Tangentially biased orbits at small radii can occur through the destruction or ejection of stars on high-eccentricity orbits that pass near the BH. There are now 17 galaxies for which we have measurements of orbital anisotropies; most come from the dynamical models presented here, but similar results are found using other orbit superposition studies (M32, van der Marel et al. 1998; Verolme et al. 2002; NGC 4342, Cretton & van den Bosch 1999; IC 1459, Cappellari et al. 2002). Spherical theoretical models predict a range of both central cusps and anisotropies. Three models that have been studied are adiabatic BH growth (Quinlan, Hernquist, & Sigurdsson 1995), fall-in of a single BH (Nakano & Makino 1999), and BH binary models (Quinlan & Hernquist 1997). The adiabatic models grow the BH by slow accretion of material (gas or stars). The BH fall-in models start with a galaxy without a BH, and then a BH is placed at large radii where it subsequently falls in as a result of dynamical friction. The BH binary model assumes that the galaxy has an existing BH at the center and then a second BH falls in as a result of dynamical friction, and they

subsequently form a binary BH. The models predict a different value of the central anisotropy: single BH infall models have $1 > \sigma_r/\sigma_t > 0.87$, adiabatic models have $\sigma_r/\sigma_t \approx 0.87$, and BH binary models have $\sigma_r/\sigma_t \approx 0.7$. The increased tangential anisotropy for the binary models is due to the orbital motion of the binary in the galaxy core, which causes it to affect more stars on radial orbits.

The models that agree best with both observed anisotropies and density slopes depend on the type of galaxy, whether it is a core or power law. Examining the solid points in Figure 12, one notices that those galaxies with shallow central densities have the largest tangential motion. The central σ_r/σ_t for core galaxies is around 0.4 (highly tangentially biased), while that for the power-law galaxies ranges from 0.45 to 1.05 with an average of 0.8. Thus, it appears that the core galaxies are more consistent with the BH binary models, and the power-law galaxies are more consistent with adiabatic growth. These conclusions are similar to those of Faber et al. (1997) and Ravindranath, Ho, & Filippenko (2002). Unfortunately, these comparison models are limited by their simplistic initial conditions (i.e., isotropic velocity dispersion tensor, spherical potential). Fortunately, the large number of researchers working in this area now (e.g., Milosavljevic & Merritt 2001; Holley-Bockelmann et al. 2002) will provide improved theoretical comparisons.

4.8. *The Need for Three Integrals*

It is important to know whether the distribution function of these galaxies depends on three integrals of motion or only on the two classical integrals (energy and z-component of angular momentum). In two-integral models the dispersion in the R- and z-directions must be equal (where R, ϕ, z are the usual cylindrical coordinates). Figure 13 plots this ratio for the 12 galaxies. There are no obvious radial trends. For seven galaxies, at small radii the radial dispersion is higher than in the θ-direction. For two, the θ motion significantly dominates there. At other radii, the results show a variety of trends with some galaxies having rising ratios and others having falling ones. The *average* ratio along the major axis is close to unity (i.e., a two-integral model), but the radial run demonstrates that the best-fit model is inconsistent with having only two integrals of the motion. This result is similar to that found in other orbit-based models (Verolme et al. 2002; Cappellari et al. 2002).

We discussed that most of the galaxies (10 of the 12) have substantial tangential motion near their centers, but not whether this is due to the θ or ϕ motion. By comparison of Figure 13 to Figure 10, we notice that at most of the radii, the curves are similar, which implies that the θ and ϕ dispersions are similar. However, Figure 13 shows a significant increase in the contribution from the θ-direction near their centers for only two of the galaxies, whereas from Figure 10 we see that most galaxies show a dramatic increase in the tangential motion near their centers. Thus, the dominant component in nearly all of the galaxies near the center is in the ϕ-direction. At the center, the ϕ dispersion generally has similar contributions from random and ordered motion. The theoretical models discussed in § 4.7 do not provide the difference between the θ and ϕ dispersions, but these could potentially be important constraints.

4.9. *Possible Concerns*

Our models are limited to axisymmetry. Triaxial and nonsymmetric structures may be common attributes of galaxies. Of the 12 galaxies in this sample, at least four (NGC 3377, NGC 3608, NGC 4473, and NGC 7457) show signs of nonaxisymmetric structure in the kinematics. An incorrect assumption of axisymmetry could bias our results. For example, if a bar is observed down its long axis, the radial streaming motions along the bar may increase the projected velocity dispersion. This measured increase may mimic that expected with a central mass concentration (Gerhard 1988). We have not investigated the effects of triaxiality on BH mass determinations in detail, but we believe that these effects average to zero when the system is viewed from many different orientations; thus, triaxiality may contribute to the scatter in our mass determinations but should not produce a systematic bias. Furthermore, the scatter due to not considering triaxiality may be a function of galaxy size, since large core galaxies possibly are more triaxial than the smaller power-law galaxies. Clearly, triaxial models should be used to quantify these effects. Any bias caused by using an inappropriate stellar distribution could be more dramatic if we only had data at larger radii where the stellar potential needs to be included. However, as seen in Figure 8, the ground-based data alone do a fairly good job at measuring the BH mass compared to when including the *HST*. Thus, at least at the level of our uncertainties, the BH mass is unaffected by using the large radial data, suggesting that if the galaxies are not axisymmetric, then either the nonaxisymmetry is unimportant for the modeling or it is constant with radius. The best way to test biases with the axisymmetry assumption is either to model the same galaxies with triaxial codes or to run the axisymmetric code on an analytic triaxial galaxy.

We have assumed that the surfaces of constant luminosity density in all of our galaxies are similar spheroids (with the exception of NGC 4473, where we add a disk component). This assumption is consistent with the observation that the ellipticity of the surface brightness distribution is similar at all radii, but other density distributions are also consistent with this observation. The question is whether the assumption of spheroidal equidensity surfaces could bias our BH mass determinations. Some guidance comes from the analysis of Magorrian & Ballantyne (2001), who study the influence of embedded stellar disks. In this case, they find that face-on disks in round galaxies in projection may bias a spherical model toward having radial anisotropy. This effect is primarily seen at large radii and is unlikely to bias the BH mass since we are measuring the kinematics so close to the BH. However, this effect may be important for the orbital structure that we measure in these galaxies. Again, at small radii, the influence of a disk is likely to be small since we do not see strong signatures of one (except in NGC 4473); however, it would be difficult to measure a disk at larger radii. Thus, there is a concern that we may be biased by this effect in some of the galaxies at larger radii. Fortunately, only four of our galaxies are rounder than E3, so this is unlikely to alter the overall conclusions. There are many other possibilities other than embedded stellar disks that can lead to nonuniqueness in the deprojection. The best way to understand their effects is to run models with different deprojections. For four of the galaxies, we have tried a variety of inclinations and find insignificant changes to both the BH mass and orbital structure.
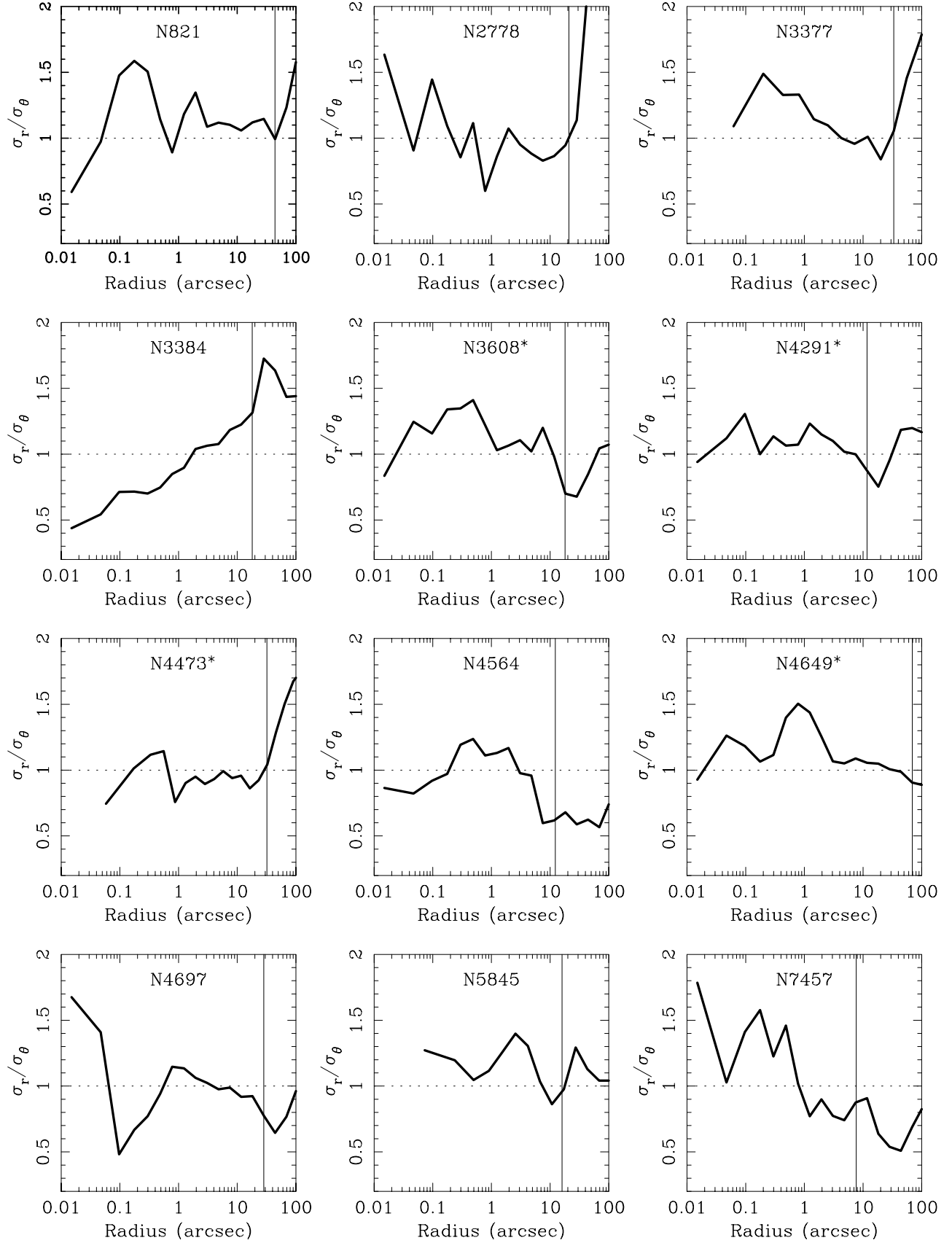
FIG. 13.—Ratio of the radial to the θ velocity dispersion for all 12 galaxies plotted as a function of radius along the equator for the best-fit model (*solid line*). The dotted line is at $\sigma_r/\sigma_\theta = 1$, which is the result along the major axis for a two-integral model. The galaxies show a range of profiles with no obvious radial trends. The vertical solid line is the radial extent of the ground-based data; results beyond that radius are not meaningful. An asterisk denotes whether the galaxy is a core galaxy.

We have not included a dark halo in this analysis. It appears that in most elliptical galaxies the dark halo becomes important at about the half-light radius (Krona-witter et al. 2000; Rix et al. 1997). Even though we have data and model results at these large radii, and they are plotted in Figure 10, we do not use the model results from these radii because they may be seriously comprised by the exclusion of a dark halo. At radii less than $R_e/4$ the stars and central BH dominate the potential. For Figure 12 we choose $R_e/4$; at this radius the stellar potential dominates. The BH mass is determined almost exclusively by the small-radii data; thus, we are confident that exclusion of a dark halo is unimportant for the BH mass estimate. Gebhardt et al. (2000a) include various dark-halo profiles and find little difference in the results inside of $R_e/2$. The next step in the data analysis is to run models in order to measure both the BH mass and dark halo properties.

We have assumed that the mass-to-light ratio is constant with radius. As we discuss above, the exclusion of a dark halo is unlikely to affect either the BH mass or the orbital structure; however, variation at small radii can have an effect. For example, a dramatic increase in the stellar mass-to-light ratio in the central regions can decrease the measured BH mass if not accounted for. We have not done a detailed spectral analysis to determine the stellar makeup, but we can use the color gradients to provide some constraints. For the 12 galaxies, the *largest* mass-to-light variation from $10''$ to the center is $V-I = 0.1$; the average is around 0.04. Models of Worthey (1994) suggest that $V-I = 0.1$ implies a mass-to-light change of about 20%. We do not include that small variation here but note that Gebhardt et al. (2000a) use an even larger variation and find no change in the measured BH mass. Cappellari et al. (2002) find a similar result for IC 1459. Thus, we conclude that inclusion of a small mass-to-light variation at small radius will have an insignificant effect on the BH mass.

5. CONCLUSIONS

The 12 galaxies in this paper all have significant BH detections, with a typical statistical significance in the masses of around 30%. The average significance of detection is well above 99%, and the least significant detection (NGC 2778) has about 90% confidence. Thus, for this sample, every galaxy has a BH. In fact, only one nearby galaxy with high-resolution spectral data lacks any significant BH detection: the pure disk galaxy M33 (Gebhardt et al. 2001). The most obvious difference between M33 and the galaxies with significant BH detection is that the latter have a bulge component.

For a few of these galaxies, ground-based spectra alone yield reasonably precise BH masses. The masses based on ground-based data alone are generally remarkably close to the masses based on ground-based and *HST* data; there is no evidence that masses based on ground-based data alone are systematically high. The most important aspect of using ground-based data is to assure that the models are fitted using full generality (i.e., without assumptions about the orbital structure).

The most significant correlation with BH mass is with the velocity dispersion. The present intrinsic scatter is around 0.23 dex in BH mass (Tremaine et al. 2002). It will be

extremely illuminating to include more galaxies at both extremes, the low- and high-mass ends. The next most significant correlation is with the radial to tangential velocity dispersion at $R_e/4$. We do not know whether this is simply a secondary correlation due to that with the velocity dispersion or if it represents an evolutionary pattern due to the growth of the BH. Detailed theoretical and N-body models are required to understand this. The BH mass also significantly correlates with both galaxy bulge luminosity and bulge mass, but neither of these is as strong as with dispersion.

The uncertainties in the BH masses reported here are only statistical. We have not attempted to include uncertainties from the assumptions in our models or systematic errors in our analysis outlined in § 4.9. We believe that the increase in the uncertainties is likely to be small, but additional tests are required in order to substantiate this. We can use the $M_{\rm BH}/\sigma$ correlation as an approximate constraint on the uncertainties. If there is an underlying physical mechanism that causes a *perfect* correlation between $M_{\rm BH}$ and σ, then any scatter seen in the correlation must be measurement error. Since the current scatter is comparable to the measurement error, we probably have a reasonable estimate of our uncertainties; any additional uncertainties caused by our assumptions should be smaller than 0.23 dex in BH mass. However, this argument applies only to random errors. If, for example, galaxies deviate from our assumptions systematically, then the $M_{\rm BH}/\sigma$ correlation may still have small scatter but incorrect BH masses. The only way to test this is to include a larger sample with general dynamical models that cover a wide variety of input configurations.

The orbit-based models provide a look into the internal orbital structure of an axisymmetric system. Based on the small sample of galaxies shown here and the limited theoretical comparisons, we are already able to place some constraints on the possible evolutionary history of the galaxy. The results in this paper suggest that core galaxies have tangentially biased orbits near their centers, while power-law galaxies show a range of tangential relative to radial motion. As suggested by Faber et al. (1997) and Ravindranath et al. (2002), it appears that the core galaxies are consistent with the BH/binary models, and the power-law galaxies are more consistent with adiabatic growth. This conclusion comes from analysis of the stellar surface brightness profiles, and now a similar conclusion comes from the stellar kinematics. Significant improvement in our understanding of the orbital structure will come from data sets with two-dimensional kinematics. De Zeeuw et al. (2002) and Bacon et al. (2002) present examples of data sets that can be exploited for this analysis. However, in order to make progress in this area we must understand possible systematic biases that can arise from various assumptions (e.g., dark halo, different deprojections, lack of axial symmetry, etc.)

APPENDIX

FOS AND GROUND-BASED DATA FOR NGC 3377 AND NGC 5845

The ground-based velocities and dispersions for NGC 3377 come from Kormendy et al. (1998) and will not be repeated here. Since our models use the LOSVDs, we convert from the first two moments to the velocity profile using Monte Carlo simulations. Each velocity profile realization is a Gaussian with the mean chosen from a random draw from the measured mean using its uncertainty and the σ chosen from a random draw from the measured dispersion using its uncertainty. This procedure does not take into account the H3 and H4 components that are likely to be nonzero. However, the model results depend very little on the higher order moments, since it is mainly the radial run of the first two moments that determines the BH mass. The height of the LOSVD at a given velocity is then the mean of the simulations, and the uncertainty is given by the 68% confidence bands of the simulations.

For NGC 5845, the data were taken with the MDM telescope. The observational setup and reductions are similar to those outlined in Pinkney et al. (2002). We used the Ca II triplet region around 8500 Å. The plate scale is 0″.59 pixel^{-1}. The wavelength scale is 1.44 Å pixel^{-1}, with an instrumental resolution of 0.75 Å or 26 km s^{-1}. We observed along three position angles for NGC 5845: 0°, 22°, and 90° (defined from the major axis to the minor axis), with total exposure times of 3 hr for each position angle (9 hr in total). In Table 4 we report the first four velocity moments of the LOSVD for the three position angles. They are plotted in Figure 14.

For the FOS data, the reduction procedure is similar to that in Gebhardt et al. (2000a). Both galaxies were observed using the 0″.21 square aperture. The wavelength range, 4566–6815 Å, includes the Mg I b lines near 5175 Å. The spectral dispersion is 1.09 Å pixel^{-1}. The instrumental velocity dispersion is $\sigma_{\mathrm{instr}} = \mathrm{FWHM}/2.35 = 1.76 \pm 0.03$ pixels $= 101 \pm 2$ km s^{-1} (internal
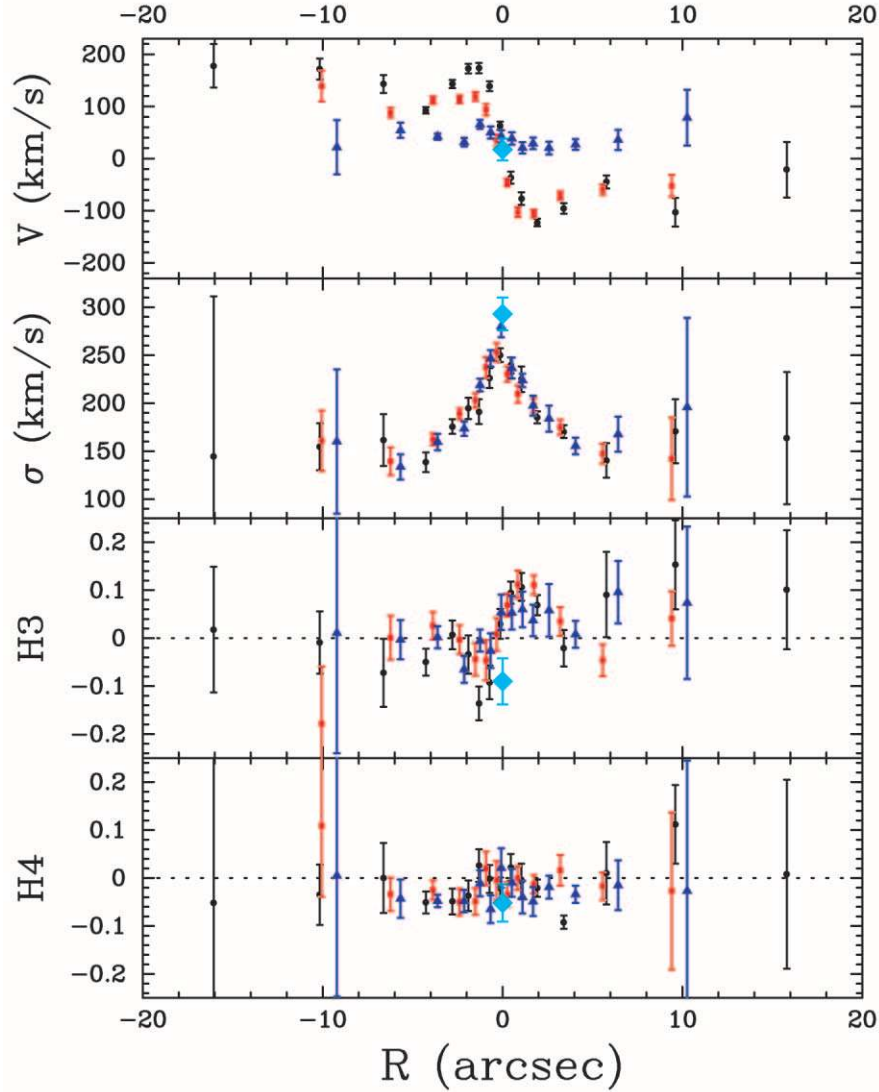

FIG. 14.—First four moments of the LOSVD for NGC 5845 along three different position angles. The black circles are along the major axis. The red squares are along the axis 20° up from the major axis, and the blue triangles are along the minor axis. The light-blue diamonds represent the first four moments of the single FOS pointing that we have at the center.

TABLE 4
KINEMATIC DATA FOR NGC 3377 AND NGC 5845

P.A. (deg)	Radius (arcsec)	Velocity (km s⁻¹)	σ (km s⁻¹)	H3	H4
		HST/FOS Kinematics for NGC 3377			
0....................	0.00	0.0 ± 6.5	258.0 ± 6.0	−0.05 ± 0.02	0.00 ± 0.02
	−0.20	100.0 ± 5.0	215.0 ± 5.0	−0.06 ± 0.02	−0.01 ± 0.02
		HST/FOS Kinematics for NGC 5845			
0....................	0.00	17.2 ± 20.8	292.9 ± 17.0	−0.09 ± 0.05	−0.05 ± 0.04
		Ground-based Kinematics for NGC 5845			
0....................	−0.13	63.0 ± 7.8	250.0 ± 7.2	0.03 ± 0.03	−0.02 ± 0.02
	0.46	−36.6 ± 11.5	239.4 ± 8.3	0.10 ± 0.02	0.02 ± 0.03
	1.05	−76.7 ± 12.2	224.9 ± 13.3	0.11 ± 0.03	−0.01 ± 0.04
	1.93	−122.6 ± 7.3	185.2 ± 6.3	0.07 ± 0.02	−0.02 ± 0.02
	3.41	−95.8 ± 10.1	170.3 ± 6.7	−0.02 ± 0.04	−0.09 ± 0.01
	5.77	−44.9 ± 12.3	140.4 ± 18.1	0.09 ± 0.09	0.01 ± 0.07
	9.60	−103.0 ± 27.3	170.7 ± 33.5	0.15 ± 0.09	0.11 ± 0.08
	15.80	−21.3 ± 53.3	163.5 ± 68.9	0.10 ± 0.12	0.01 ± 0.20
	−0.72	138.7 ± 9.4	226.2 ± 10.4	−0.09 ± 0.04	−0.00 ± 0.03
	−1.31	173.4 ± 9.8	191.2 ± 12.9	−0.14 ± 0.04	0.03 ± 0.03
	−1.90	172.5 ± 9.1	194.5 ± 11.1	−0.03 ± 0.04	−0.04 ± 0.03
	−2.79	143.1 ± 7.9	175.7 ± 7.6	0.01 ± 0.03	−0.05 ± 0.03
	−4.26	92.6 ± 6.2	138.4 ± 10.3	−0.05 ± 0.03	−0.05 ± 0.02
	−6.62	142.9 ± 17.1	161.6 ± 27.0	−0.07 ± 0.07	0.00 ± 0.07
	−10.16	171.7 ± 20.2	154.6 ± 24.6	−0.01 ± 0.07	−0.04 ± 0.06
22.................	−0.33	34.7 ± 11.4	253.0 ± 9.8	0.01 ± 0.03	−0.01 ± 0.04
	0.26	−45.8 ± 8.1	230.4 ± 8.1	0.07 ± 0.02	−0.04 ± 0.03
	0.85	−102.8 ± 9.6	209.6 ± 9.1	0.11 ± 0.03	0.00 ± 0.03
	1.74	−105.7 ± 7.8	197.7 ± 7.2	0.11 ± 0.02	−0.01 ± 0.02
	3.21	−71.0 ± 8.5	175.0 ± 8.1	0.04 ± 0.03	0.02 ± 0.03
	5.57	−59.4 ± 10.2	147.2 ± 10.4	−0.05 ± 0.03	−0.02 ± 0.03
	9.41	−52.2 ± 20.9	142.0 ± 43.1	0.04 ± 0.06	−0.03 ± 0.16
	−0.92	93.6 ± 10.9	237.2 ± 10.9	−0.05 ± 0.04	0.02 ± 0.04
	−1.51	119.3 ± 8.7	203.0 ± 7.6	−0.04 ± 0.03	−0.05 ± 0.03
	−2.39	113.9 ± 7.6	189.0 ± 5.8	−0.00 ± 0.03	−0.05 ± 0.03
	−3.87	112.1 ± 7.2	162.4 ± 6.4	0.03 ± 0.03	−0.03 ± 0.02
	−6.23	87.8 ± 9.7	139.4 ± 14.5	0.00 ± 0.05	−0.03 ± 0.04
	−10.06	139.1 ± 29.7	160.7 ± 31.7	−0.18 ± 0.12	0.11 ± 0.15
90.................	0.07	42.6 ± 11.7	280.1 ± 11.4	0.05 ± 0.04	0.02 ± 0.04
	0.66	49.8 ± 11.7	246.6 ± 8.6	−0.03 ± 0.04	−0.07 ± 0.03
	1.25	65.5 ± 8.7	218.8 ± 6.6	−0.01 ± 0.02	−0.01 ± 0.03
	2.13	31.5 ± 8.3	173.5 ± 7.5	−0.07 ± 0.03	−0.05 ± 0.02
	3.61	42.0 ± 6.1	159.5 ± 8.6	0.00 ± 0.02	−0.05 ± 0.01
	5.67	54.3 ± 14.6	133.6 ± 13.2	−0.00 ± 0.04	−0.04 ± 0.04
	9.21	21.9 ± 52.0	160.0 ± 75.3	0.01 ± 0.25	0.01 ± 0.25
	−0.52	38.5 ± 12.0	236.5 ± 11.0	0.05 ± 0.04	−0.01 ± 0.03
	−1.11	20.6 ± 10.9	223.8 ± 6.9	0.06 ± 0.04	−0.04 ± 0.03
	−1.70	29.2 ± 11.0	197.3 ± 10.4	0.04 ± 0.03	−0.05 ± 0.03
	−2.59	20.2 ± 12.3	183.9 ± 13.6	0.06 ± 0.06	−0.02 ± 0.02
	−4.06	27.1 ± 10.3	155.4 ± 8.7	0.01 ± 0.03	−0.03 ± 0.02
	−6.42	35.9 ± 19.3	167.6 ± 18.3	0.10 ± 0.07	−0.01 ± 0.05
	−10.26	78.5 ± 53.7	195.8 ± 93.1	0.07 ± 0.16	−0.03 ± 0.27

error). This width is intrinsic to the instrument and is not strongly affected by how the aperture is illuminated (Keyes et al. 1995). We therefore make no aperture illumination corrections to the measured velocity dispersion. Flat-fielding and correction for geomagnetically induced motions (GIMs) were done as in Kormendy et al. (1996). The flat-field image uses the same aperture. Each galaxy exposure is divided into multiple subintegrations during the visits. There are four individual exposures for NGC 5845 with a total integration time of 2.43 hr. For NGC 3377, the central pointing had a single exposure of 0.66 hr and two flanking exposures on both sides of the galaxy of 1.02 and 0.90 hr (each split into two subintegrations).

The most important step is to determine where the slit was actually placed. For NGC 3379 (Gebhardt et al. 2000a), this was a critical issue since the aperture was not placed exactly in the center of the galaxy. For both NGC 3377 and NGC 5845, the aperture placement is much more secure since both galaxies have central cusps. Since we take a setup image of the galaxy

before the spectral observations, we know where the aperture was placed. For both galaxies, the center of the galaxy is at the center of the FOS aperture to better than $0\rlap{.}''05$. For NGC 3377, we have two additional apertures placed $0\rlap{.}''2$ away from the center along the major axis on opposite sides. We have checked their placement using the setup images and confirm that they were both placed at the requested position to within $0\rlap{.}''05$. Since the flanking spectra were placed at very similar radii on opposite sides of the galaxy, we have fitted the same velocity profile, but appropriately flipped, to both spectra. This fit is the same as that done for all of the other data used in the models. Table 4, therefore, only reports the moments for one profile fitted to both spectra.

We have three template stars taken with the same FOS aperture, and all three provide similar results for the kinematics. Table 4 includes the Gauss-Hermite moments for the single pointing for NGC 5845 and the two pointings for NGC 3377.

Extraction of the LOSVD for the three *HST* spectra and the ground-based spectra uses the procedure described by Gebhardt et al. (2000a) and Pinkney et al. (2002). We use the full LOSVD in the models, but we report only its first four moments in Table 4.

REFERENCES

Alam, S. M. K., & Ryden, B. S. 2002, ApJ, 570, 610
Bacon, R., et al. 2002, in ASP Conf. Ser., Galaxies: The Third Dimension, ed. M. Rosado, L. Binnette, & L. Arias (San Francisco: ASP), in press
Baggett, W. E., Baggett, S. M., & Anderson, K. S. J. 1998, AJ, 116, 1626
Bernardi, M., et al. 2002, AJ, submitted
Bower, G., et al. 2001, ApJ, 550, 75
Cappellari, M., et al. 2002, ApJ, 578, 787
Cretton, N., de Zeeuw, P. T., van der Marel, R. P., & Rix, H.-W. 1999, ApJS, 124, 383
Cretton, N., Rix, H.-W., & de Zeeuw, P. T. 2000, ApJ, 536, 319
Cretton, N., & van den Bosch, F. 1999, ApJ, 514, 704
de Vaucouleurs, G., de Vaucouleurs, A., Corwin, H. G., Buta, R. J., Paturel, G., & Fouquè, P. 1991, Third Reference Catalogue of Bright Galaxies (New York: Springer)
de Zeeuw, P. T., et al. 2002, MNRAS, 329, 513
Faber, S., Wegner, G., Burstein, D., Davies, R., Dressler, A., Lynden-Bell, D., & Terlevich, R. 1989, ApJS, 69, 763
Faber, S. M., et al. 1997, AJ, 114, 1771
Ferrarese, L., & Merritt, D. 2000, ApJ, 539, L9
Fisher, D., Illingworth, G., & Franx, M. 1995, ApJ, 438, 539
Gebhardt, K., et al. 1996, AJ, 112, 105
————. 2000a, AJ, 119, 1157
————. 2000b, ApJ, 539, L13
————. 2001, AJ, 122, 2469
Gerhard, O. 1988, MNRAS, 232, 13P
Gerhard, O., & Binney, J. 1996, MNRAS, 279, 993
Ho, L. C., Filippenko, A. V., & Sargent, W. L. W. 1995, ApJS, 98, 477
Holley-Bockelmann, K., Mihos, J. C., Sigurdsson, S., Hernquist, L., & Norman, C. 2002, ApJ, 567, 817
Jaffe, W., Ford, H., O'Connell, R., van den Bosch, F., & Ferrarese, L. 1994, AJ, 108, 1567
Jørgensen, I., Franx, M., & Kjærgaard, P. 1996, MNRAS, 280, 167
Keyes, C. D., et al. 1995, FOS Instrument Handbook (Baltimore: STScI)
Kochanek, C., & Rybicki, G. 1996, MNRAS, 280, 1257
Kormendy, J., Bender, R., Evans, A., & Richstone, D. 1998, AJ, 115, 1823
Kormendy, J., & Gebhardt, K. 2001, in The 20th Texas Symposium on Relativistic Astrophysics, ed. H. Martel & J. C. Wheeler (New York: AIP), 363–381
Kormendy, J., & Richstone, D. 1995, ARA&A, 33, 581

Kormendy, J., et al. 1996, ApJ, 459, L57
————. 2002, ApJ, submitted
Kronawitter, A., Saglia, R. P., Gerhard, O., & Bender, R. 2000, A&AS, 144, 53
Lauer, T. R. 1985, ApJS, 57, 473
Lauer, T. R., Faber, S. M., Ajhar, E. A., Grillmair, C. J., & Scowen, P. A. 1998, AJ, 116, 2263
Lauer, T. R., et al. 1995, AJ, 110, 2622
————. 2002, AJ, 124, 1975
Lucy, L. B. 1974, AJ, 79, 745
Magorrian, J., & Ballantyne, D. 2001, MNRAS, 322, 702
Magorrian, J., et al. 1998, AJ, 115, 2285
Merritt, D., & Ferrarese, L. 2001, MNRAS, 320, L30
Milosavljevic, M., & Merritt, D. 2001, ApJ, 563, 34
Nakano, T., & Makino, J. 1999, ApJ, 510, 155
Peletier, R. F., Davies, R. L., Illingworth, G. D., & Davies, L. E. 1990, AJ, 100, 1091
Pinkney, J., et al. 2002, ApJ, submitted
Quinlan, G., & Hernquist, L. 1997, NewA, 2, 533
Quinlan, G., Hernquist, L., & Sigurdsson, S. 1995, ApJ, 440, 554
Ravindranath, S., Ho, L. C., & Filippenko, A. V. 2002, ApJ, 566, 801
Ravindranath, S., Ho, L. C., Peng, C., Filippenko, A. V., & Sargent, W. 2001, AJ, 122, 653
Richardson, W. H. 1972, J. Opt. Soc. Am., 62, 55
Richstone, D. O., & Tremaine, S. 1984, ApJ, 286, 27
Rix, H.-W., de Zeeuw, P. T., Cretton, N., van der Marel, R. P., & Carollo, M. 1997, ApJ, 488, 702
Tonry, J., Blakeslee, J., Ajhar, E., & Dressler, A. 2000, ApJ, 530, 625
Tremaine, S., et al. 2002, ApJ, 574, 740
van der Marel, R. P., Cretton, N., de Zeeuw, P. T., & Rix, H.-W. 1998, ApJ, 493, 613
Verdoes Kleijn, G., van der Marel, R. P., Carollo, C. M., & de Zeeuw, P. T. 2000, AJ, 120, 1221
Verolme, E., & de Zeeuw, P. T. 2002, MNRAS, 331, 959
Verolme, E., et al. 2002, MNRAS, 335, 517
Wahba, G. 1990, Spline Models for Observational Data (Philadelphia: SIAM)
Worthey, G. 1994, ApJS, 95, 107